ADVANCES IN ATMOSPHERIC SCIENCES, VOL. 40, MAY 2023, 856–873

• **Original Paper** •

Comparative Analysis of the Generalized Omega Equation and Generalized Vertical Motion Equation※

Baofeng JIAO[1], Lingkun RAN[*1], Na LI[1], Ren CAI[2], Tao QU[2], and Yushu ZHOU[1]

[1]*Institute of Atmospheric Physics*, *Chinese Academy of Sciences*, *Beijing* 100029, *China*

[2]*Urumqi City Bureau of Meteorology*, *Urumqi* 830002, *China*

(Received 15 December 2021; revised 11 April 2022; accepted 4 May 2022)

ABSTRACT

Research on vertical motion in mesoscale systems is an extraordinarily challenging effort. Allowing for fewer assumptions, a new form of generalized vertical motion equation and a generalized Omega equation are derived in the Cartesian coordinate system (nonhydrostatic equilibrium) and the isobaric coordinate system (hydrostatic equilibrium), respectively. The terms on the right-hand side of the equations, which comprise the $\boldsymbol{Q}$ vector, are composed of three factors: dynamic, thermodynamic, and mass. A heavy rain event that occurred from 18 to 19 July 2021 in southern Xinjiang was selected to analyze the characteristics of the diagnostic variable in the generalized vertical motion equation ($\boldsymbol{Q}_z$) and the diagnostic variable in the generalized Omega equation ($\boldsymbol{Q}_p$) using high-resolution model data. The results show that the horizontal distribution of the $\boldsymbol{Q}_z$-vector divergence at 5.5 km is roughly similar to the distribution of the $\boldsymbol{Q}_p$-vector divergence at 500 hPa, and that both relate well to the composite radar reflectivity, vertical motion, and hourly accumulated precipitation. The $\boldsymbol{Q}_z$-vector divergence is more effective in indicating weak precipitation. In vertical cross sections, regions with alternating positive and negative large values that match the precipitation are mainly concentrated in the middle levels for both forms of $\boldsymbol{Q}$ vectors. The temporal evolutions of vertically integrated $\boldsymbol{Q}_z$-vector divergence and $\boldsymbol{Q}_p$-vector divergence are generally similar. Both perform better than the classical quasigeostrophic $\boldsymbol{Q}$ vector and nongeostrophic $\boldsymbol{Q}$ vector in indicating the development of the precipitation system.

Key words: generalized Omega equation, generalized vertical motion equation, $\boldsymbol{Q}$ vector, heavy rain

Citation: Jiao, B. F., L. K. Ran, N. Li, R. Cai, T. Qu, and Y. S. Zhou, 2023: Comparative analysis of the generalized Omega equation and generalized vertical motion equation. *Adv. Atmos. Sci.*, **40**(5), 856–873, https://doi.org/10.1007/s00376-022-1435-5.

Article Highlights:

- $\boldsymbol{Q}_z$ contains more thermodynamic and mass information than $\boldsymbol{Q}_p$.
- Both $\boldsymbol{Q}_z$ and $\boldsymbol{Q}_p$ relate well to the vertical velocity and rainband, and $\boldsymbol{Q}_z$ is more effective at indicating weak precipitation.

1. Introduction

Vertical motion is one of the key factors affecting the occurrence and development of high-impact weather, in that it is closely related to water vapor condensation, the release of potential instability, energy conversion, and kinetic and thermodynamic exchange between the upper troposphere and lower troposphere (Zhu et al., 2007; Yue, 2014; Gao and Zhou, 2019; Ran et al., 2019). Analyzing and researching vertical motion has continued to be a challenging area of meteorology.

Vertical velocity is difficult to directly measure, thus, it is usually obtained based on the determination of other physical quantities. The forcing mechanism of vertical motion is generally obtained by solving the vertical motion equation. Hoskins et al. (1978) derived the $\boldsymbol{Q}$ vector divergence as the only forcing term in the quasigeostrophic vertical motion equation, and it can indicate the vertical motion of baroclinic weather systems. Henceforth, the quasigeostrophic $\boldsymbol{Q}$ vector has been widely used in the determination of the characteristics of synoptic-scale systems and the dynamic interpretation of numerical prediction products (Strahl and Smith, 2001; Dixon et al., 2003).

Considering the inherent differences between subsynoptic and mesoscale systems, in terms of the magnitude of their vertical velocities, the significance of their non-

※ This paper is a contribution to the special issue on the 14th International Conference on Mesoscale Convective Systems and High-Impact Weather.

* Corresponding author: Lingkun RAN
Email: rlk@mail.iap.ac.cn

geostrophic characteristics, and the influences of their diabatic heating effects, static stability variations in the horizontal direction, and nonuniform saturations (Vasilj and Smith, 1997; Gao et al., 2004; Yang et al., 2007), $\boldsymbol{Q}$-vector theory has been expanded through related studies. As a result, different forms of $\boldsymbol{Q}$ vectors with fewer assumptions have been proposed. For example, the semigeostrophic $\boldsymbol{Q}$ vector (Hoskins and Draghici, 1977) and nongeostrophic $\boldsymbol{Q}$ vector (Davies-Jones, 1991) take the nongeostrophic property of real atmosphere into consideration, moist $\boldsymbol{Q}$ vector (Yao et al., 2004), $\boldsymbol{C}$ vector (Xu, 1992), and generalized $\boldsymbol{Q}$ vector (Räisänen, 1995; Rantanen et al., 2017; Li, 2018) discuss the vertical motion characteristics of absolute dry air (Davies-Jones, 1991), moist saturated air (Yue et al., 2013), and saturated and unsaturated transition zones (Gao et al., 2013; Ran et al., 2019), respectively. Furthermore, these different forms of $\boldsymbol{Q}$-vector divergence are widely used in the diagnostic analysis of heavy rain events. Cao et al. (2008) pointed out that the separated rotational and divergent component $\boldsymbol{Q}$ vectors improved the dynamic identification of both the location of rainstorm and the direction of rainband. Yue et al. (2013) applied the moist $\boldsymbol{Q}$-vector interpretation technique to produce quantitative precipitation forecasts, and the results showed effective improvement of the test scores and forecast accuracy for precipitation of different orders. Ran et al. (2019) showed that the $\boldsymbol{Q}$ vector based on 24-h forecast data from the Global Forecasting System (GFS) has a close relationship with the observed 6-h precipitation. Currently, high-resolution numerical models are being widely used. It is necessary to obtain high-resolution data that are consistent between kinematics and thermodynamics. Li (2018) applied a generalized vertical motion equation to high-resolution model data and found that the vertical velocity calculated through iterative computation was similar to the vertical velocity output directly from the model. Even so, hydrostatic equilibrium is included in pressure coordinates.

From the above discussion, it can be seen that $\boldsymbol{Q}$-vector theory research has produced many conclusions from vertical motion diagnosis and analysis. However, new vertical motion equations with fewer assumptions are still needed to describe the development of vertical motion and reveal the associated mechanism for subsynoptic and mesoscale systems. Gao and Zhou (2019) also pointed out that the vertical motion equation still needs to be assessed for its applicability in severe mesoscale systems. Besides, most of the work on vertical motion equations occurs within the framework of hydrostatic equilibrium, which is not valid for smaller mesoscale systems (meso-beta to meso-gamma). In this context, the aim of this study is to derive new forms of generalized vertical motion equations that hold with fewer assumptions and better approximate the real atmosphere, i.e., the generalized vertical motion equation within the nonhydrostatic equilibrium framework of the local Cartesian coordinate system and a generalized Omega equation under the hydrostatic equilibrium framework of the isobaric coordinate system. Both equations are based on the primitive equations with the generalized potential temperature (Gao et al., 2004) taken into consideration to describe non-uniform saturated moist air.

A heavy rain event that occurred during 18–19 July 2021 in southern Xinjiang and was successfully reproduced in a high-resolution numerical simulation is used to evaluate the new vertical motion equations. The model output data are used to compare the new forms of vertical motion equations, focusing on the relationship between the $\boldsymbol{Q}$-vector divergence and composite radar reflectivity, vertical movement, and hourly accumulated precipitation to reveal the typical differences. The remainder of the paper is structured as follows: Section 2 details the generalized vertical motion equations. In section 3, the selected case is described. The model configuration is given in section 4. The results and discussion are presented in section 5, and the conclusions are summarized in section 6.

2. Generalized vertical motion equations

Because of rapid improvements in model spatiotemporal resolutions, numerical weather prediction models can currently resolve more small-scale (notably, convection) features, for which assumptions of large-scale motion are generally no longer valid. Therefore, the need exists to develop new forms of generalized vertical motion equations based on fewer restrictive assumptions which are more suitable for mesoscale and subsynoptic systems. Since the earlier versions of vertical motion equations are mainly in the isobaric coordinate system, a new form of generalized Omega equation in isobaric coordinates is derived first. Generally, there are three main differences between the new and the earlier versions. Firstly, the generalized potential temperature is introduced to represent the non-uniform saturated moist air. Secondly, the material derivative of the thermal wind imbalance vector is retained, which typically vanishes if the Alternative Balance (Davies-Jones, 1991) is adopted. Thirdly, the terms on the left side of the generalized Omega equation are related to Omega while the right ones are not. Therefore, the variation of vertical velocity can be captured instead of the accurate magnitude and direction, which depend on waveform solution assumption. Furthermore, a new form of vertical motion equation in Cartesian coordinates is derived, and it is not constrained by hydrostatic equilibrium in the vertical direction. The new forms of the generalized vertical motion equations and their diagnostic variables are discussed in greater detail in Appendices A and B.

2.1. *Generalized vertical motion equation*

In the local Cartesian coordinate system, the generalized vertical motion equation can be written as follows (see Appendix A for details):

$$\frac{\partial}{\partial z}(h\sigma_z)\left(\frac{\partial^2 w}{\partial x^2}+\frac{\partial^2 w}{\partial y^2}\right)+f_0\frac{\partial^2 w}{\partial z^2}+\left[-\frac{\partial^2 v}{\partial z^2}+\frac{\partial}{\partial z}\left(2h\frac{\partial \sigma_z}{\partial x}+\sigma_z\frac{\partial h}{\partial x}\right)\right]\frac{\partial w}{\partial x}+\left[\frac{\partial^2 u}{\partial z^2}+\frac{\partial}{\partial z}\left(2h\frac{\partial \sigma_z}{\partial y}+\sigma_z\frac{\partial h}{\partial y}\right)\right]\frac{\partial w}{\partial y}+\left[-\frac{\partial^2 \zeta}{\partial z^2}+\frac{\partial^2}{\partial z\partial y}\left(h\frac{\partial \sigma_z}{\partial y}\right)+\frac{\partial^2}{\partial z\partial x}\left(h\frac{\partial \sigma_z}{\partial x}\right)\right]w=-\left(\frac{\partial q_{zx1}}{\partial x}+\frac{\partial q_{zy1}}{\partial y}\right)-\left(\frac{\partial q_{zx2}}{\partial x}+\frac{\partial q_{zy2}}{\partial y}\right)-\left(\frac{\partial q_{zx3}}{\partial x}+\frac{\partial q_{zy3}}{\partial y}\right)+f_0\frac{\partial M_z}{\partial z}, \quad (1)$$

where $\sigma_z=c_p(\partial\theta^*/\partial z)/(c_v f_0\eta)$ represents static stability. The diagnostic variables can be expanded as:

$$q_{zx1}=-\left(\frac{\partial^2 v}{\partial t\partial z}+u\frac{\partial^2 v}{\partial x\partial z}+v\frac{\partial^2 v}{\partial y\partial z}\right)+\frac{\partial v}{\partial z}\frac{\partial u}{\partial x}-\frac{\partial u}{\partial z}\frac{\partial v}{\partial x}, \quad (2)$$

$$q_{zx2}=\frac{\partial}{\partial z}\left\{h\frac{c_p}{c_v f_0}\left[\frac{\partial}{\partial x}\left(\frac{1}{\eta}\frac{\partial\theta^*}{\partial t}\right)+u\frac{\partial}{\partial x}\left(\frac{1}{\eta}\frac{\partial\theta^*}{\partial x}\right)+v\frac{\partial}{\partial x}\left(\frac{1}{\eta}\frac{\partial\theta^*}{\partial y}\right)\right]-h\frac{c_p}{c_v}\frac{\partial\theta}{\partial y}\right\}+\frac{c_p h}{c_v f_0}\frac{\partial}{\partial z}\left[\frac{1}{\eta}\left(\frac{\partial u}{\partial x}\frac{\partial\theta^*}{\partial x}+\frac{\partial v}{\partial x}\frac{\partial\theta^*}{\partial y}\right)\right]+\frac{c_p}{c_v f_0\eta}\frac{\partial h}{\partial z}\left(\frac{\partial u}{\partial x}\frac{\partial\theta^*}{\partial x}+\frac{\partial v}{\partial x}\frac{\partial\theta^*}{\partial y}\right), \quad (3)$$

$$q_{zx3}=-h\frac{\partial}{\partial x}[\sigma_z(\lambda-M_z)]-\frac{\partial v}{\partial z}M_z, \quad (4)$$

$$q_{zy1}=\frac{\partial^2 u}{\partial t\partial z}+u\frac{\partial^2 u}{\partial x\partial z}+v\frac{\partial^2 u}{\partial y\partial z}+\frac{\partial v}{\partial z}\frac{\partial u}{\partial y}-\frac{\partial u}{\partial z}\frac{\partial v}{\partial y}, \quad (5)$$

$$q_{zy2}=\frac{\partial}{\partial z}\left\{\frac{c_p h}{c_v f_0}\left[\frac{\partial}{\partial y}\left(\frac{1}{\eta}\frac{\partial\theta^*}{\partial t}\right)+u\frac{\partial}{\partial y}\left(\frac{1}{\eta}\frac{\partial\theta^*}{\partial x}\right)+v\frac{\partial}{\partial y}\left(\frac{1}{\eta}\frac{\partial\theta^*}{\partial y}\right)\right]+h\frac{c_p}{c_v}\frac{\partial\theta}{\partial x}\right\}+\frac{c_p h}{c_v f_0}\frac{\partial}{\partial z}\left[\frac{1}{\eta}\left(\frac{\partial u}{\partial y}\frac{\partial\theta^*}{\partial x}+\frac{\partial v}{\partial y}\frac{\partial\theta^*}{\partial y}\right)\right]+\frac{c_p}{c_v f_0\eta}\frac{\partial h}{\partial z}\left(\frac{\partial u}{\partial y}\frac{\partial\theta^*}{\partial x}+\frac{\partial v}{\partial y}\frac{\partial\theta^*}{\partial y}\right), \quad (6)$$

$$q_{zy3}=-h\frac{\partial}{\partial y}[\sigma_z(\lambda-M_z)]+\frac{\partial u}{\partial z}M_z. \quad (7)$$

In Eq. (1), $\boldsymbol{Q}_{z1}=(q_{zx1},q_{zy1})$, $\boldsymbol{Q}_{z2}=(q_{zx2},q_{zy2})$, and $\boldsymbol{Q}_{z3}=(q_{zx3},q_{zy3})$ are the dynamic $\boldsymbol{Q}$ vector, thermodynamic $\boldsymbol{Q}$ vector, and mass $\boldsymbol{Q}$ vector, respectively, representing the dynamic forcing, thermodynamic forcing, and mass forcing for the vertical motion. A list of symbols is presented in Table 1.

2.2. *Generalized Omega equation*

In the isobaric coordinate system, the generalized Omega equation can be written as follows (see Appendix B for the details):

$$\frac{\partial^2}{\partial x^2}(\sigma_p\omega)+\frac{\partial^2}{\partial y^2}(\sigma_p\omega)-f_0\frac{\partial^2\omega}{\partial p^2}+\frac{\partial\omega}{\partial x}\frac{\partial^2 v}{\partial p^2}-\frac{\partial\omega}{\partial y}\frac{\partial^2 u}{\partial p^2}+\frac{\partial^2\zeta}{\partial p^2}\omega=-\left(\frac{\partial q_{px1}}{\partial x}+\frac{\partial q_{py1}}{\partial y}\right)-\left(\frac{\partial q_{px2}}{\partial x}+\frac{\partial q_{py2}}{\partial y}\right)-\left(\frac{\partial q_{px3}}{\partial x}+\frac{\partial q_{py3}}{\partial y}\right)-f_0\frac{\partial M_p}{\partial p}, \quad (8)$$

where $\zeta=\frac{\partial v}{\partial x}-\frac{\partial u}{\partial y}$ represents vertical vorticity and $\sigma_p=\frac{h}{f_0\eta}\frac{\partial\theta^*}{\partial p}$ represents static stability. The diagnostic variables are:

$$q_{px1}=\frac{\partial^2 v}{\partial p\partial t}+u\frac{\partial^2 v}{\partial p\partial x}+v\frac{\partial^2 v}{\partial p\partial y}+\frac{\partial u}{\partial p}\frac{\partial v}{\partial x}-\frac{\partial v}{\partial p}\frac{\partial u}{\partial x}, \quad (9)$$

Table 1. List of symbols.

Symbols	Meanings
u	Zonal wind component
u_g	Zonal geostrophic wind component
v	Meridional wind component
v_g	Meridional geostrophic wind component
w	Vertical wind component
ω	Vertical wind component
v_h	Horizontal wind velocity vector
f_0	Constant reference Coriolis parameter
p	Pressure
p_s	Surface pressure
ϕ	Geopotential
α	Specific volume
ρ	Density
g	Gravitational acceleration
θ	Potential temperature
θ^*	Generalized potential temperature
η	Latent heat function
L_v	Specific latent heat of vaporization
q_s	Saturation specific humidity
q_v	Specific humidity
T	Absolute temperature
H	Heating rate
R	Gas constant
c_p	Heat capacity at constant pressure
c_v	Specific heat for a constant-volume process
σ_z	Static stability parameter
σ_p	Static stability parameter
ζ	Vertical vorticity component

$$q_{px2} = \frac{h}{f_0}\left[\frac{\partial}{\partial x}\left(\frac{1}{\eta}\frac{\partial \theta^*}{\partial t}\right) + u\frac{\partial}{\partial x}\left(\frac{1}{\eta}\frac{\partial \theta^*}{\partial x}\right) + v\frac{\partial}{\partial x}\left(\frac{1}{\eta}\frac{\partial \theta^*}{\partial y}\right) + \frac{1}{\eta}\left(\frac{\partial u}{\partial x}\frac{\partial \theta^*}{\partial x} + \frac{\partial v}{\partial x}\frac{\partial \theta^*}{\partial y}\right)\right] - h\frac{\partial \theta}{\partial y}, \quad (10)$$

$$q_{px3} = \frac{\partial v}{\partial p}M_p, \quad (11)$$

$$q_{py1} = -\frac{\partial^2 u}{\partial p \partial t} - u\frac{\partial^2 u}{\partial p \partial x} - v\frac{\partial^2 u}{\partial p \partial y} - \frac{\partial v}{\partial p}\frac{\partial u}{\partial y} + \frac{\partial u}{\partial p}\frac{\partial v}{\partial y}, \quad (12)$$

$$q_{py2} = \frac{h}{f_0}\left[\frac{\partial}{\partial y}\left(\frac{1}{\eta}\frac{\partial \theta^*}{\partial t}\right) + u\frac{\partial}{\partial y}\left(\frac{1}{\eta}\frac{\partial \theta^*}{\partial x}\right) + v\frac{\partial}{\partial y}\left(\frac{1}{\eta}\frac{\partial \theta^*}{\partial y}\right) + \frac{1}{\eta}\left(\frac{\partial u}{\partial y}\frac{\partial \theta^*}{\partial x} + \frac{\partial v}{\partial y}\frac{\partial \theta^*}{\partial y}\right)\right] + h\frac{\partial \theta}{\partial x}, \quad (13)$$

$$q_{py3} = -\frac{\partial u}{\partial p}M_p. \quad (14)$$

In Eq. (8), $\boldsymbol{Q}_{p1} = (q_{px1}, q_{py1})$, $\boldsymbol{Q}_{p2} = (q_{px2}, q_{py2})$, and $\boldsymbol{Q}_{p3} = (q_{px3}, q_{py3})$ are the dynamic $\boldsymbol{Q}$ vector, thermodynamic $\boldsymbol{Q}$ vector, and mass $\boldsymbol{Q}$ vector, respectively, in the isobaric coordinate system, representing the dynamic forcing, thermodynamic forcing, and mass forcing for the vertical motion.

Equations (1) and (8) are diagnostic equations that describe vertical motion. Through the terms on the right-hand side of the equations, the physical factors that affect vertical motion on the left-hand side can be analyzed. Equation (1) is based on the nonhydrostatic equilibrium dynamic framework of the local Cartesian coordinate system, while Eq. (8) is based on the hydrostatic equilibrium framework of the isobaric coordinate system. The dynamic components $\boldsymbol{Q}_{z1}$ and $\boldsymbol{Q}_{p1}$ are similar, and both components contain terms for horizontal wind variation, horizontal advection, and enstrophy. However, the thermodynamic components $\boldsymbol{Q}_{z2}$ and $\boldsymbol{Q}_{p2}$ are quite different. In addition to the quasi-frontogenesis term, $\boldsymbol{Q}_{z2}$ also contains the vertical gradient of quasi-frontogenesis, which introduces more thermodynamic information. There is no mass forcing if the atmosphere is strictly incompressible. In this case, $\boldsymbol{Q}_{p3}$ is always zero, while $\boldsymbol{Q}_{z3}$ still contains the effect of horizontal divergence. Overall, the Q vector in the generalized vertical motion equation based on the local Cartesian coordinate system contains more information in the thermodynamic and mass terms.

In the derivation of Eqs. (1) and (8), the generalized potential temperature (Gao et al., 2004) is introduced. Since the generalized potential temperature contains the latent heat of condensation, it seamlessly connects the potential temperature and the equivalent potential temperature into a single conservative form. Therefore, Eq. (1) and Eq. (8) do not explicitly include diabatic forcing, and the calculation is simple. However, local changes are introduced at the same time due to the retainment of the material derivative of the thermal wind imbalance vector. From the diagnosis result, the temporal tendency terms are less important than the other terms, such as the advection terms, so they can be omitted in the calculation process without affecting the overall distribution and main characteristics of the result. If a balance approximation like the "Alternative Balance" (Davies-Jones, 1991) is adopted, these local change items can be ignored.

To analyze the characteristics of the hydrostatic equilibrium $\boldsymbol{Q}$ vector and the nonhydrostatic equilibrium $\boldsymbol{Q}$ vector, high-resolution data output of the numerical model is used in this paper to calculate the two different forms of the $\boldsymbol{Q}$ vector. The relationships between $\boldsymbol{Q}$-vector divergence and composite radar reflectivity, vertical velocity, and hourly accumulated precipitation are determined to reveal the typical differences.

3. Case review

From 18 to 19 July 2021, precipitation covered the area from Kizilsu Kirghiz Autonomous Prefecture to the Aksu Prefecture along the southern flank of the Tianshan Mountains in southern Xinjiang. As the data from automatic weather stations show (Fig. 1), the precipitation region was mainly distributed in a northeast–southwest orientation, which is consistent with the topography. At 1200 UTC 18 July, precipitation appeared over the east slope of the high terrain, with a maximum hourly record of more than 10 mm. Subsequently, the rainband moved eastward. The maximum daily precipitation in the Kashgar Prefecture, Kezhou mountainous region, Aksu Prefecture, and parts of the western Hotan Prefecture exceeded 50 mm, causing local floods, mudslides, landslides, and other geological disasters. Serious economic losses were reported locally, including damage related to enterprise exploration equipment, residential houses, and fields.

This event was mainly affected by a midlevel shortwave trough, low-level shear line, and low-level convergence line. As shown in Fig. 2, at 1200 UTC 18 July, straight westerly airflow dominates at 200 hPa. At 500 hPa, a shortwave trough lies over the western part of Kizilsu Kirghiz Autonomous Prefecture. The rainband is within the ascending region ahead of the shortwave trough and gradually moves eastward. At the 700-hPa level, the confluence of the southwesterly and westerly airflows forms a northeast–southwestward shear line located in the northern part of Kizilsu Kirghiz Autonomous Prefecture and the western part of Aksu. The shear line is conducive to local convergence, vertical motion development, and the release of unstable energy. The near-surface flow field is uniformly from the east over the Tarim Basin. On the one hand, this airstream transports water vapor to the precipitation region; on the other hand, it helps to form a banded convergence line on the east side of the terrain, which is conducive to the development of upward motion. All these factors favor triggering local convective activity.

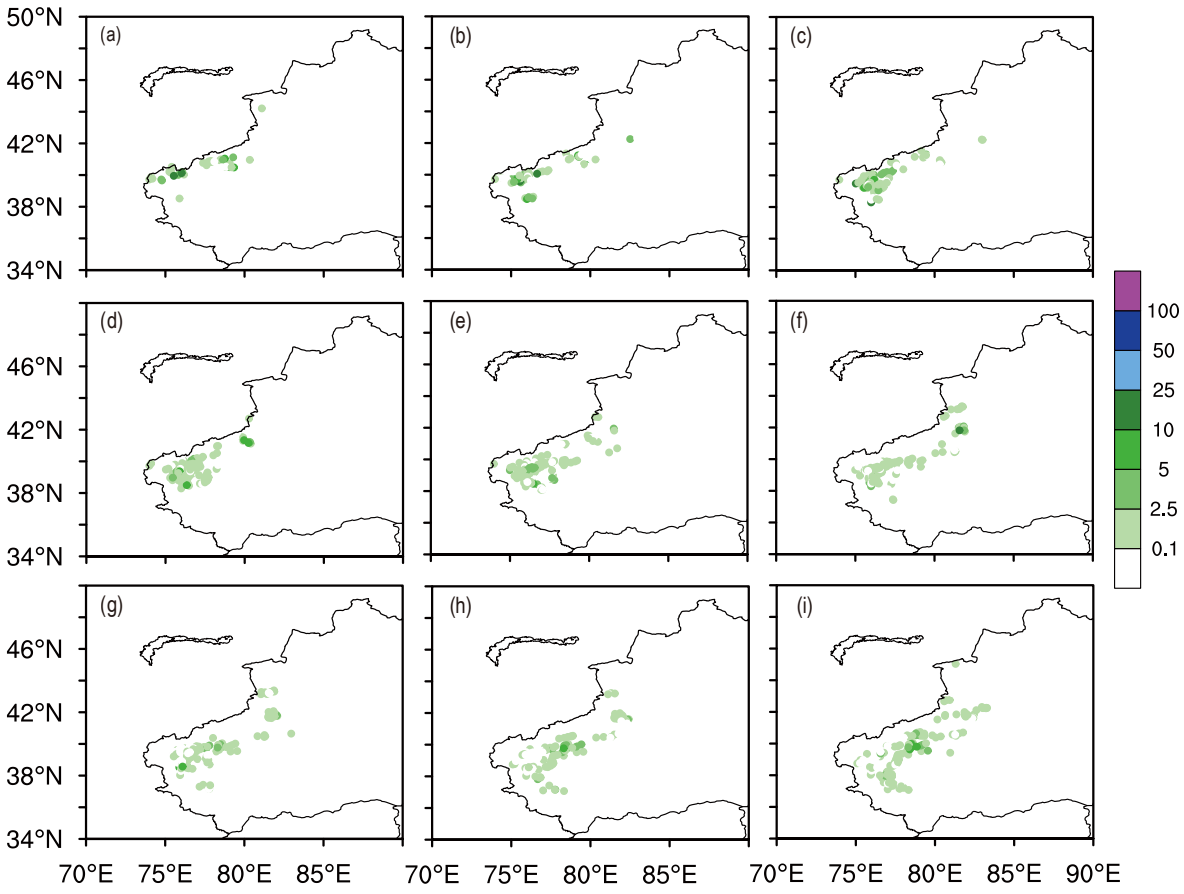

Fig. 1. Observed hourly precipitation from 1200 UTC to 2000 UTC 18 July 2021 (units: mm).

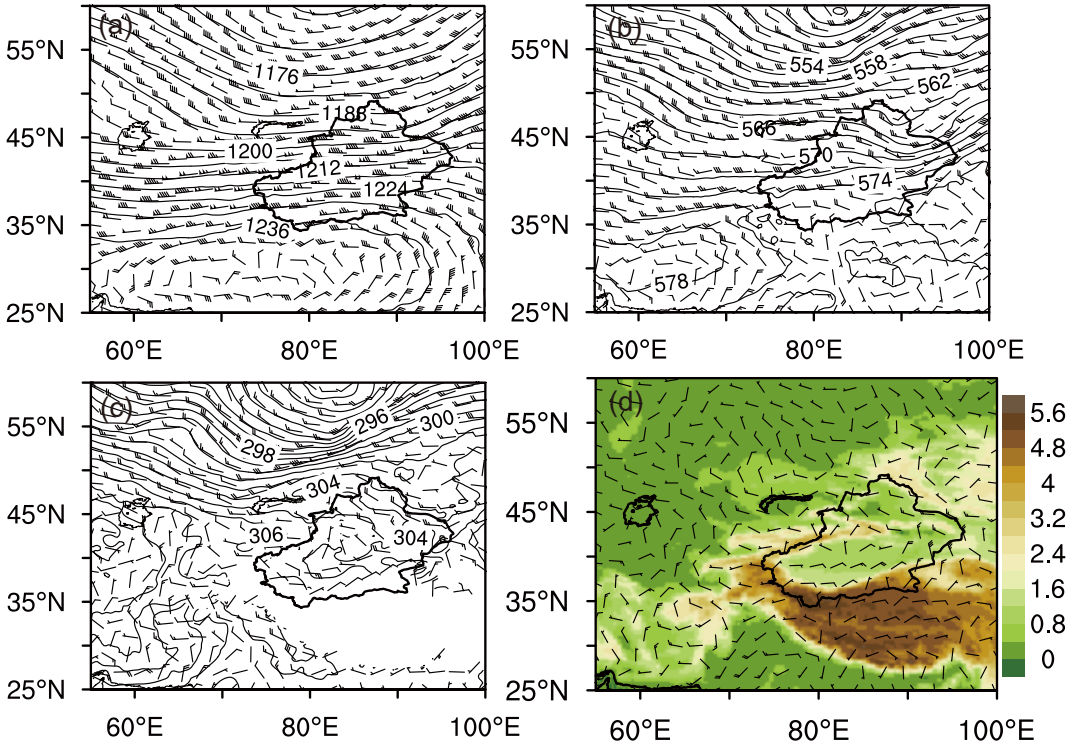

Fig. 2. (a) 200 hPa wind vector (units: m s^{-1}) and geopotential height (contour, units: ×10 gpm), (b) 500 hPa wind vector (units: m s^{-1}) and geopotential height (contour, units: ×10 gpm), (c) 700 hPa wind vector (units: m s^{-1}) and geopotential height (contour, units: ×10 gpm), and (d) terrain (shaded, units: m) and wind vector (units: m s^{-1}) at 10 m at 1200 UTC on 18 July 2021.

4. Simulation

The Weather Research and Forecasting (WRF) model is used to study this event because of its high spatial and temporal resolution. The main configuration of the experiment is shown in Table 2 and described below. The initial fields and boundary conditions adopted here are the fifth generation ECMWF reanalysis for the global climate and weather (ERA5), with a horizontal grid spacing of 0.25° × 0.25° and 38 layers in the vertical direction. The boundary conditions are provided every 3 hours. The experiment uses a single-layer grid with the center point at (37.1°N, 79.9°E). The number of grid points in the horizontal directions is 901 × 901, with a grid spacing of 3 km. There are 81 layers in the vertical direction, from the near-surface layer stretching up to 5 hPa at the model top. The physical configuration includes the RRTMG radiation scheme, the unified Noah land surface model, the WRF double moment 6-class scheme microphysics scheme, and the YSU planetary boundary layer scheme. Convective parameterization is switched off because the convection is explicitly resolved with this setup.

Figure 3 shows the comparison between the simulated 24-hour accumulated precipitation (Fig. 3a) and that observed (Fig. 3b). The observations are taken from the merged precipitation product at hourly and 0.05° latitude/longitude temporal-spatial resolution, following application of PDF (probability density function), BMA (Bayes model averaging), and OI (optimal interpolation) based on the hourly precipitation observed by national surface weather stations, automatic weather stations in China, and retrieved precipitation from CMORPH (CPC MORPHing technique) satellite data (Shen et al., 2013). Overall, the model reproduced the precipitation process well. Both the simulated and observed rainbands are northeast–southwest oriented. The precipitation coverage is the same and is mainly located in the northern part of Kashgar and the southwestern part of Aksu. In terms of intensity, the simulated precipitation center is slightly stronger than the observations. In the next section, the high-resolution data output by the model is used to determine and analyze the spatial distribution and temporal evolution of the $\boldsymbol{Q}$-vector divergence in the generalized Omega equation and the generalized vertical motion equation based on Eqs. (2)–(7) and (9)–(14).

Table 2. Summary of the model configuration in the experiment.

	Model configuration
Grid points	901 × 901
Horizontal grid spacing	3 km
Vertical levels	81
Model top	5 hPa
Microphysics	WDM6
Radiation	RRTMG
Land surface	Noah
Planetary boundary layer	YSU

5. Results

5.1. *Horizontal structure*

The distribution of $\boldsymbol{Q}$-vector fields at low levels, such as 850 hPa, has been typically analyzed in previous studies with a focus on low-altitude regions such as the southeast coast of China. Considering that the average altitude of Southern Xinjiang is ~ 3000 m, the level of 500 hPa, or 5.5 km, is chosen to conduct a comparison in this study. Figure 4 shows the horizontal distribution of $\boldsymbol{Q}$-vector divergence in the generalized Omega equation ($\boldsymbol{Q}_p$, left column) and the $\boldsymbol{Q}$-vector divergence in the generalized vertical motion equation ($\boldsymbol{Q}_z$, right column) superposed with composite radar reflectivity at different stages. The overall horizontal characteristics of the two kinds of $\boldsymbol{Q}$-vector divergence are quite similar. The high-value region with alternating positive and negative values is mainly located in the range of the 10-dBZ contour, which primarily indicates the position information and movement characteristics of the precipitation system. The area covered by high values of $\boldsymbol{Q}_z$-vector divergence is significantly larger than that covered by high values of $\boldsymbol{Q}_p$-vector divergence. For example, at 1200 UTC 18 July, the value of $\boldsymbol{Q}_z$ is large near (41.5°N, 76.5°E) within the 20-dBZ contour, which is a better indication of precipitation in the system.

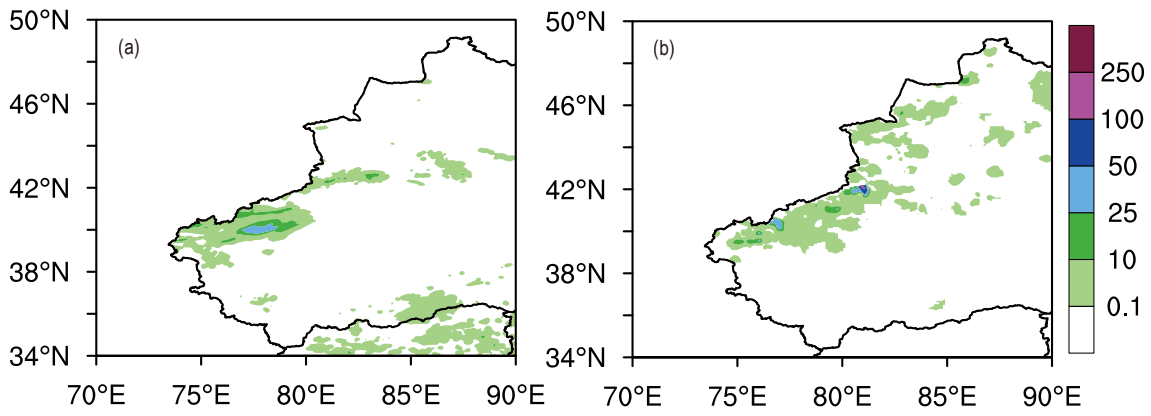

Fig. 3. (a) The simulated and (b) observed 24-hour accumulated precipitation (units: mm) from 0000 UTC 18 July to 0000 UTC 19 July 2021.

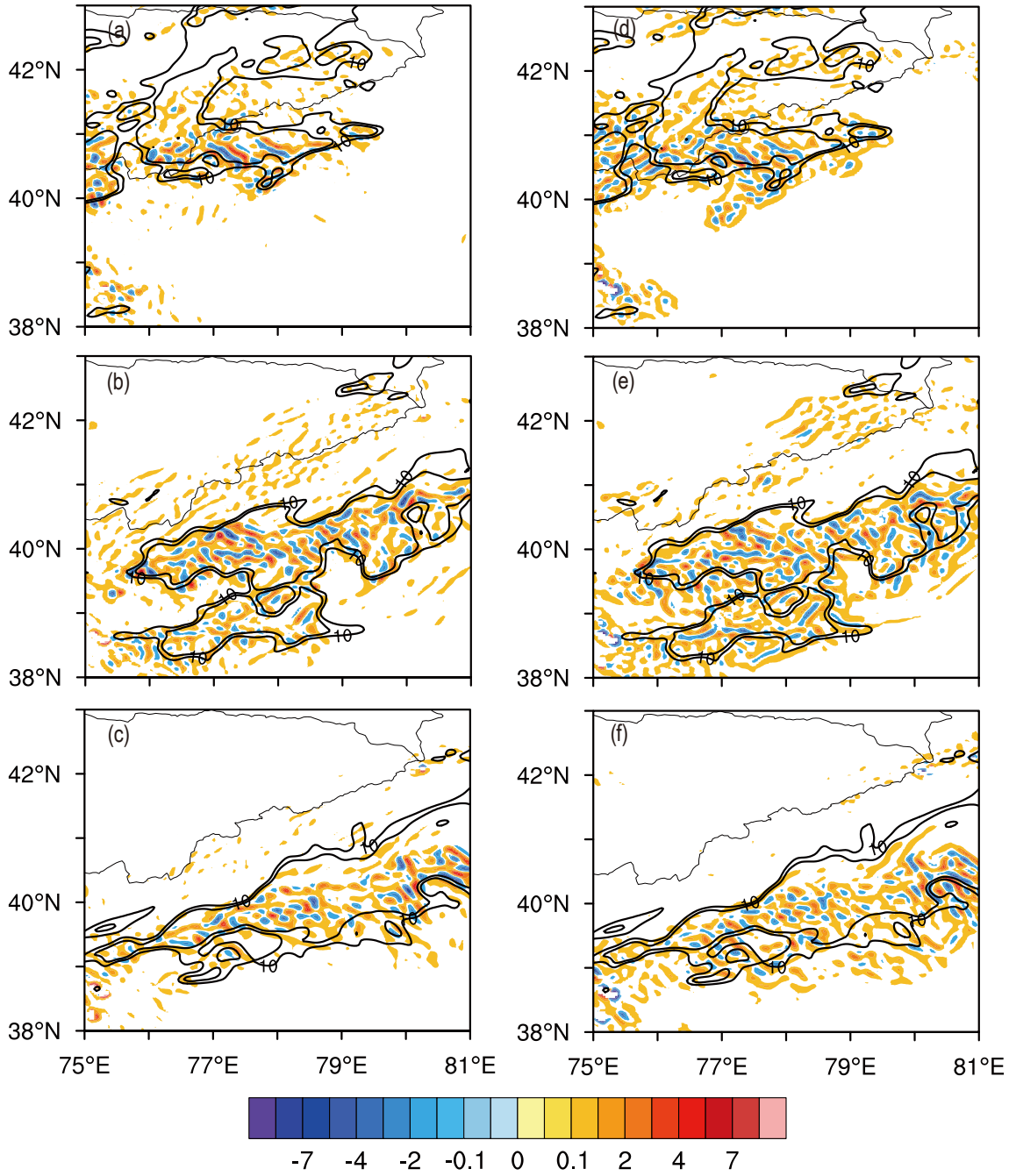

Fig. 4. Horizontal distribution of $\boldsymbol{Q}$-vector divergence at 1200 UTC 18 July 2021 (a, d), 1800 UTC 18 July 2021 (b, e), and 0000 UTC 19 July 2021 (c, f), where (a–c) represent the $\boldsymbol{Q}_p$-vector divergence (units: 10^{-8} Pa^{-1} s^{-2}) at 500 hPa and (d–f) indicate the $\boldsymbol{Q}_z$-vector divergence (units: 10^{-6} m^{-1} s^{-2}) at 5.5-km height. The black line is composite radar reflectivity (units: dBZ).

However, some high-value regions of $\boldsymbol{Q}_z$ also appear outside of the 10-dBZ contour at the same time, such as near (40°N, 77°E), which indicates a certain risk of false alarm. In other words, there is no precipitation corresponding to the regions mentioned above with abnormal $\boldsymbol{Q}$-vector divergence. Similar instances of false alarms have been found in previous research. This is partly because vertical motions in the atmosphere are not entirely produced by $\boldsymbol{Q}$-vector (quasi-geostrophic) forcing and partly because physical processes closely related to the development of precipitation systems, such as evaporation, are not considered. In practical application, it is usually necessary to combine other factors into comprehensive consideration, which is beyond the scope of this paper. The horizontal characteristics at 1800 UTC 18 July and at 0000 UTC 19 July are also basically similar. The horizontal distributions of the two forms of $\boldsymbol{Q}$-vector divergence correspond well with the composite radar reflectivity. In particular, the area covered by high values of $\boldsymbol{Q}_z$ is much larger, consistent with the analysis above.

The three components of $\boldsymbol{Q}_p$ were analyzed, and the

results show that the distribution of $\boldsymbol{Q}_p$-vector divergence depends almost exclusively on the second term, the thermodynamic forcing term. Further analysis of $\boldsymbol{Q}_{p2}$ reveals that the key process is:

$$q_{pkx} = \frac{h}{f_0}\left[u\frac{\partial}{\partial x}\left(\frac{1}{\eta}\frac{\partial\theta^*}{\partial x}\right)+v\frac{\partial}{\partial x}\left(\frac{1}{\eta}\frac{\partial\theta^*}{\partial y}\right)\right], \tag{15}$$

$$q_{pky} = \frac{h}{f_0}\left[u\frac{\partial}{\partial y}\left(\frac{1}{\eta}\frac{\partial\theta^*}{\partial x}\right)+v\frac{\partial}{\partial y}\left(\frac{1}{\eta}\frac{\partial\theta^*}{\partial y}\right)\right], \tag{16}$$

which is the coupling between the wind and the horizontal gradient of generalized potential temperature. Figure 5 compares the hourly precipitation with the horizontal distribution of simulated vertical velocity and the key components of $\boldsymbol{Q}_p$-vector divergence at 500 hPa at different stages. At 1200 UTC 18 July, precipitation is mainly located in Kyrgyzstan. Two banded structures stretch eastward and northeastward along both sides of the southern Tianshan Mountains. The vertical motion corresponds well to the precipitation on the eastern side of the Tianshan Mountains. The upward motion is more significant on the front side of the rainband, indicating

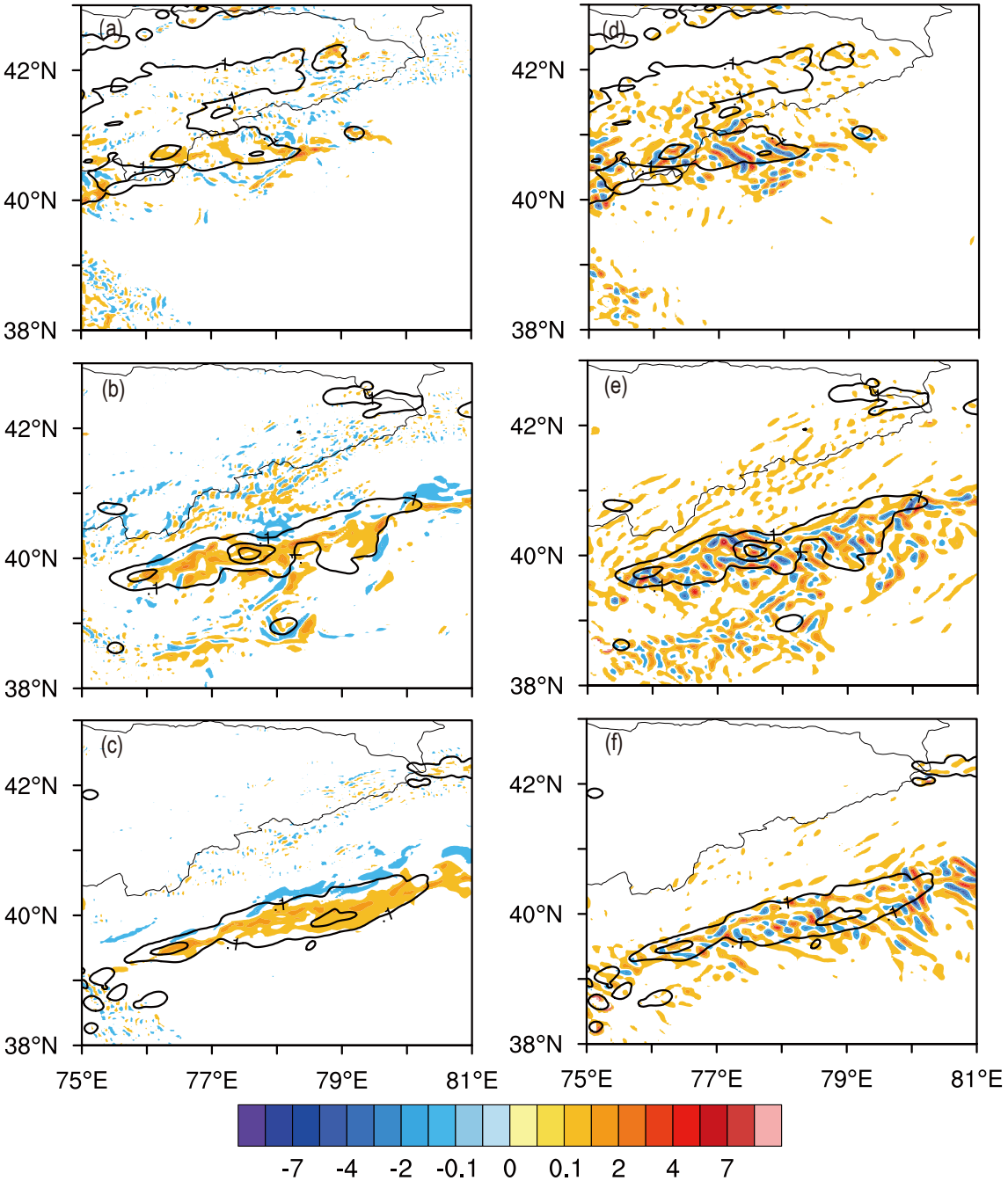

Fig. 5. Horizontal distribution of vertical velocity at 500 hPa (a–c) and the key component of $\boldsymbol{Q}_p$-vector divergence at 500 hPa (units: 10^{-8} Pa^{-1} s^{-2}) superposed with hourly precipitation (units: mm) (e–f) at 1200 UTC 18 July 2021 (a, d), 1800 UTC 18 July 2021 (b, e), and 0000 UTC 19 July 2021.

that the system continues to develop southeastward. Upon comparing with Fig. 4, it is evident that the key component basically determines the structure and variation of $\boldsymbol{Q}_p$-vector divergence, namely at 500 hPa, and the key component is correlated with the vertical motion, with the high-value region mainly distributed within the precipitation area on the eastern side of the Tianshan Mountains. This demonstrates that $\boldsymbol{Q}_p$ can track the precipitation system and the direction of movement. At 1800 UTC, the rainband moved to the western part of the Taklimakan Desert, stretched northeast–southwest, and increased significantly in intensity. At the same time, the strongest updrafts are mainly located inside the precipitation region. In addition, an elongated banded updraft appears ahead of the rainband extending southwestward. The composite radar reflectivity in Fig. 4 ahead of the rainband is associated with a corresponding updraft at the same location. The key component helps indicate the specific regions with large vertical velocities. At 0000 UTC 19 July, the precipitation system continued to move southward. The updraft is mainly collocated with the rainband, while the sinking motion is mainly located behind the rainband. Correspondingly, the high-value regions of the key component are mainly located within and on the front side of the rainband, indicating the development and movement direction of the system.

Similarly, the analysis of $\boldsymbol{Q}_z$ reveals the key process is:

$$q_{zkx} = \frac{\partial}{\partial z}\left\{h\frac{c_p}{c_v f_0}\left[u\frac{\partial}{\partial x}\left(\frac{1}{\eta}\frac{\partial\theta^*}{\partial x}\right)+v\frac{\partial}{\partial x}\left(\frac{1}{\eta}\frac{\partial\theta^*}{\partial y}\right)\right]\right\}, \quad (17)$$

$$q_{zky} = \frac{\partial}{\partial z}\left\{h\frac{c_p}{c_v f_0}\left[u\frac{\partial}{\partial y}\left(\frac{1}{\eta}\frac{\partial\theta^*}{\partial x}\right)+v\frac{\partial}{\partial y}\left(\frac{1}{\eta}\frac{\partial\theta^*}{\partial y}\right)\right]\right\}, \quad (18)$$

which contains additional vertical gradient information not considered with the key component of $\boldsymbol{Q}_p$. Figure 6 compares the hourly precipitation with the horizontal distribution of vertical velocity and the key components of $\boldsymbol{Q}_z$-vector divergence at different stages. The vertical velocity at a height of 5.5 km is analogous to that at 500 hPa. It is also found that the key component of $\boldsymbol{Q}_z$-vector divergence essentially determines the structure and variation of $\boldsymbol{Q}_z$-vector divergence. The horizontal coverage of the high value of the key component is still wider. The characteristics can be explained by the definition of the main process; q_{pkx} and q_{pky} depend only on the distribution of dynamic and thermodynamic structure at a single layer, while q_{zkx} and q_{zky} contain additional dynamic and thermodynamic information at adjacent layers because of the vertical gradient operator. For areas with weak precipitation, the value of the $\boldsymbol{Q}_z$-vector divergence is larger, such as the region near the west side of the southern part of Tianshan Mountain (41.5°N, 76°E) at 1200 UTC 18 July.

5.2. *Vertical structure*

Figure 7 shows the meridional cross-section distribution of the $\boldsymbol{Q}_p$-vector divergence (left column) and the $\boldsymbol{Q}_z$-vector divergence (right column) at different stages along 76°E. The green line represents hourly precipitation, and dark shadows represent terrain. Before precipitation occurred, the signals of both $\boldsymbol{Q}_p$-vector divergence and $\boldsymbol{Q}_z$-vector divergence in the middle and low levels are relatively weak. There are only small regions of high values in the vicinity of the terrain due to the large generalized potential temperature gradient. There is a large area of abnormal $\boldsymbol{Q}_p$-vector divergence at upper layers near 250 hPa, which does not indicate the occurrence and development of the precipitation system. The value of $\boldsymbol{Q}_z$-vector divergence at the corresponding height is small.

At 1200 UTC 18 July, the hourly precipitation is mainly distributed between 40°N and 42°N, and the center of heavy precipitation mainly appears near 40.6°N. There are obvious large values of $\boldsymbol{Q}$-vector divergences above the precipitation in the middle and low layers. The positive and negative phases of the two $\boldsymbol{Q}$-vector divergences are spatially different, but the coverage of the high-value region is similar, which correlates well with the development of the precipitation system. As before, there are still large regions of high-value $\boldsymbol{Q}_p$-vector divergence at the upper layers, which have a weaker relationship with precipitation, while the $\boldsymbol{Q}_z$-vector divergence is always weak at the same layers. By 0000 UTC 19 July, as the precipitation system moved to the southeast, the high-value area of the $\boldsymbol{Q}$-vector divergence in the middle and low layers moved to between 38°–40°N, and the meridional coverage was slightly larger than the precipitation range.

From the above discussion and the left column of Fig. 7, it is clear that large values of $\boldsymbol{Q}_p$ fill almost the entire plane, while $\boldsymbol{Q}_z$ is sparse. Reexamining the key components in Eqs. (15)–(18), it is found that they are mainly dependent on the horizontal variation of generalized potential temperature and h. The definition of h in $\boldsymbol{Q}_p$ is $h = R(p_s/p)^{-\frac{R}{c_p}}/p$, while its definition in $\boldsymbol{Q}_z$ is $h = R/(p_s/p)^{\frac{R}{c_p}}$ (see Appendices A and B). In terms of generalized potential temperature, high values at middle levels are closely related to moist air that follows the precipitation system. High values at upper levels are related to the terrain-excited gravity waves, which are significantly weaker than those at middle levels. Because there is an extra pressure variable in the denominator, $\boldsymbol{Q}_p$ increases significantly with height, which is thought to contribute to the abnormal disturbances at upper levels.

5.3. *Temporal evolution*

From the perspective of temporal evolution (Fig. 8), the precipitation in the meridional cross section along 76°E began at approximately 0700 UTC 18 July. There were two precipitation centers located near 42°N and 40.5°N, respectively (Fig. 8a). Subsequently, the precipitation system propagated southward and gradually weakened. The position corresponding to the precipitation area has a significant upward motion (Fig. 8b). In addition, there is also a large upward motion band on the front side of the precipitation area, which is consistent with the horizontal characteristics analyzed above. Near 39°N and 43°N, there is always continuous sinking/rising movement associated with high terrain.

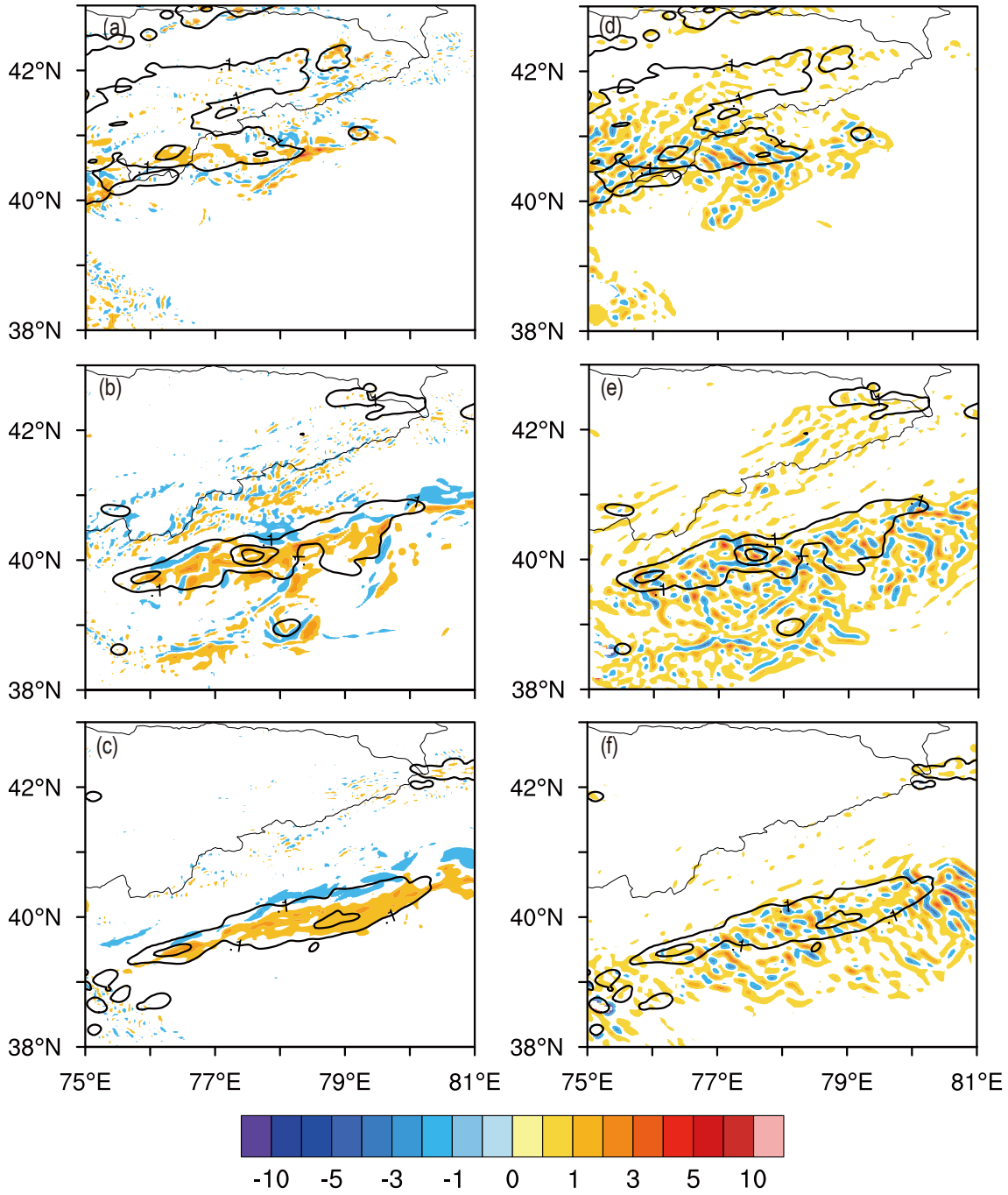

Fig. 6. Horizontal distribution of vertical velocity at 5.5 km (a–c) and the key component of $\boldsymbol{Q}_z$-vector divergence at 5.5 km (units: 10^{-6} m^{-1} s^{-2}) superposed with hourly precipitation (units: mm) (e–f) at 1200 UTC 18 July 2021 (a, d), 1800 UTC 18 July 2021 (b, e), and 0000 UTC 19 July 2021.

As shown in the previous analysis, adjacent regions of $\boldsymbol{Q}$-vector divergence with high values alternate as positive and negative. To obtain comprehensive information across several levels, the absolute values of $\boldsymbol{Q}_p$-vector divergence and $\boldsymbol{Q}_z$-vector divergence in the middle layer (600–400 hPa; 4–8 km) were vertically integrated (Figs. 8c and d). The results are quite close in terms of the evolutionary characteristics between the vertically integrated $\boldsymbol{Q}_z$- and $\boldsymbol{Q}_p$-vector divergences. The maximum value of the $\boldsymbol{Q}$-vector divergence appears 1–2 hours ahead of the precipitation, which is a good indicator of the appearance of precipitation in the area and the southward movement and development of the precipitation system. The continuous upward motion related to the terrain corresponds to a weaker vertically integrated $\boldsymbol{Q}$-vector divergence. From the temporal evolution at a single layer (Figs. 8e and f), the $\boldsymbol{Q}_z$- and $\boldsymbol{Q}_p$-vector divergences both correspond well to the precipitation area and the vertical velocity within the rainband. However, the meridional range of the larger value of the $\boldsymbol{Q}_z$-vector divergence is significantly wider, which is a good indication of the vertical motion

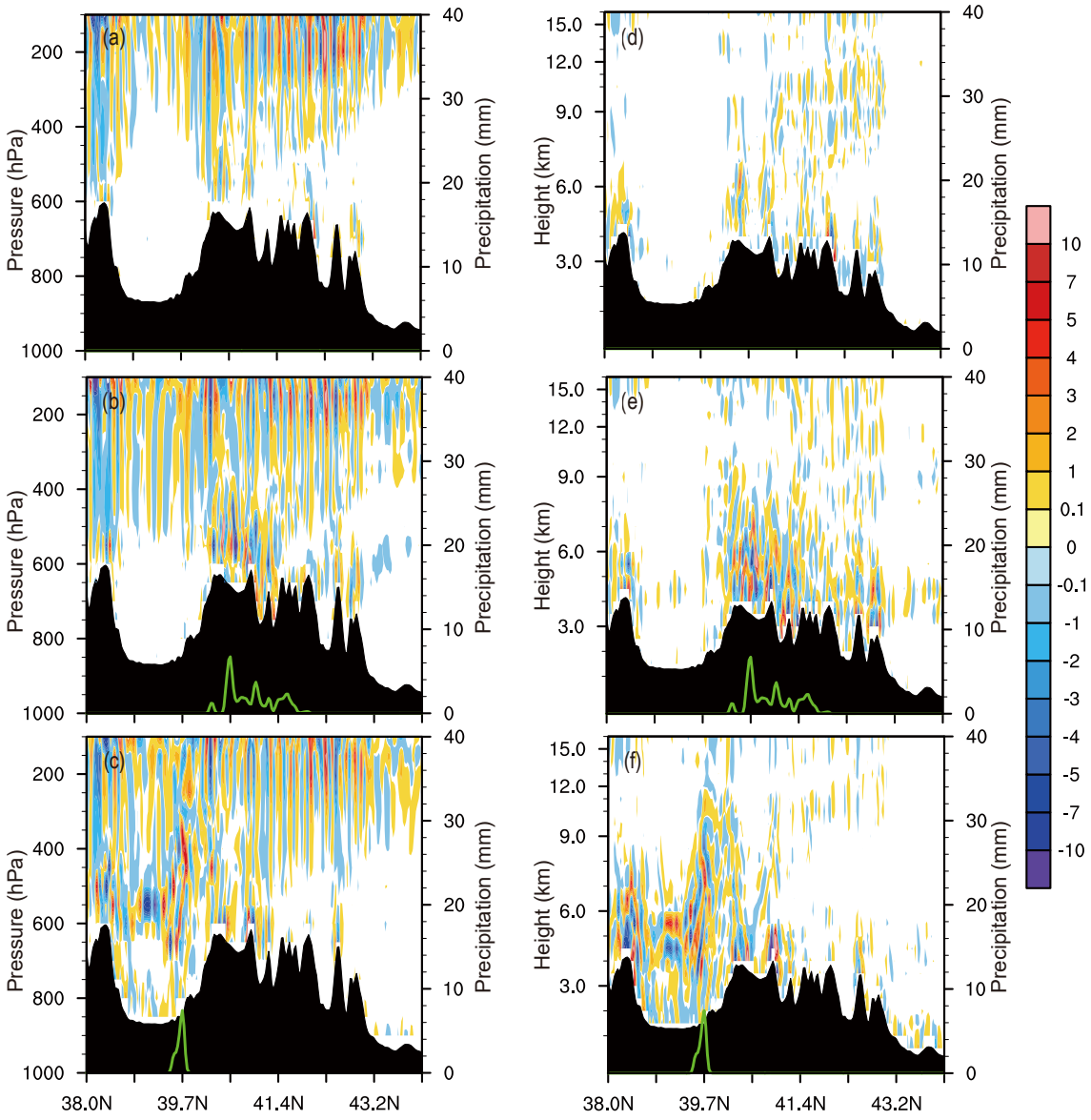

Fig. 7. Meridional cross sections of (a–c) $\boldsymbol{Q}_p$-vector divergence (units: 10^{-8} Pa^{-1} s^{-2}) and (d–f) $\boldsymbol{Q}_z$-vector divergence (units: 10^{-6} m^{-1} s^{-2}) along 78°E at (a, d) 1200 UTC 18 July, (b, e) 1800 UTC 18 July, and (c, f) 0000 UTC 19 July 2021. The green lines represent hourly precipitation (units: mm), and dark shadows represent terrain (units: km).

ahead of the rainband.

5.4. *Performance of other Q vectors*

For comparison, the horizontal and vertical structures of the quasigeostrophic $\boldsymbol{Q}$-vector divergence and nongeostrophic $\boldsymbol{Q}$-vector divergence at 1800 UTC 18 July are given in Fig. 9. At 500 hPa, the traditional QG $\boldsymbol{Q}$ vector is scattered with significant maxima inside and outside the echo region, which cannot effectively distinguish the simulated precipitation system. Whereas, the performance of the nongeostrophic $\boldsymbol{Q}$ vector is much better. The high values are mainly concentrated within the echo regions, although they cannot fully reflect the distribution characteristics of the precipitation system. The newly derived $\boldsymbol{Q}$ vectors (both $\boldsymbol{Q}_z$ and $\boldsymbol{Q}_p$) basically fill the entire echo region (Fig. 4) and have the best correspondence with the precipitation system. They both perform better than the traditional QG $\boldsymbol{Q}$ vector in indicating significance for the precipitation region and development of the system in the following few hours. From the perspective of vertical characteristics, large values are mainly concentrated near the precipitation in the middle troposphere for all diagnostic variables. The quasigeostrophic $\boldsymbol{Q}$ vector has significant false abnormal signals in non-precipitation areas, while the nongeostrophic $\boldsymbol{Q}$ vector and $\boldsymbol{Q}_p$ have false abnormal signals at the upper layers. $\boldsymbol{Q}_z$ is the best diagnostic variable in the vertical cross section since the high values are mainly near the rainband and move with the system.

Revisiting the difference in definition, the generalized $\boldsymbol{Q}$ vectors comprise the information of the actual wind field and nonuniform saturated air, as well as the gradient in both

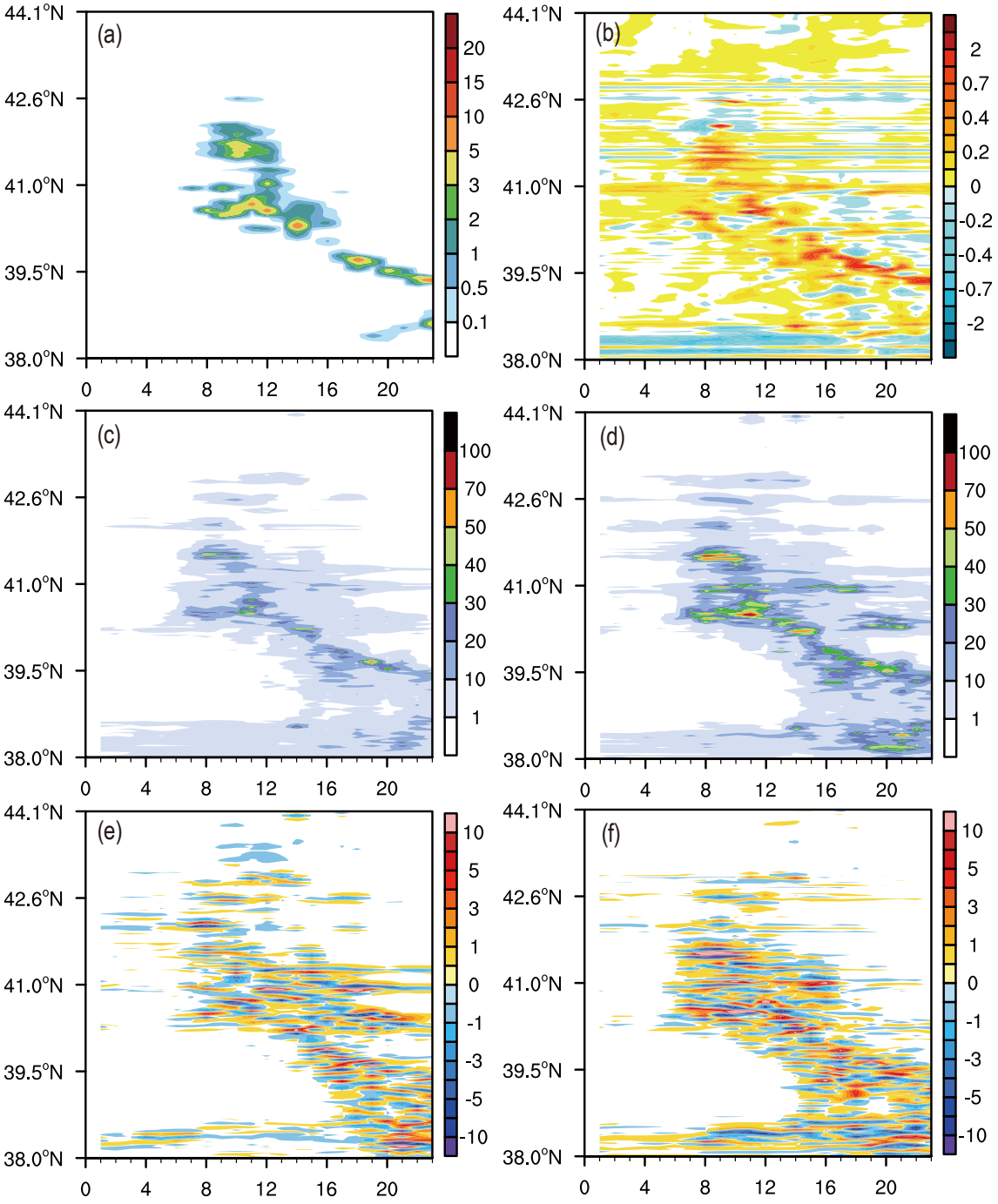

Fig. 8. Time variation in (a) hourly precipitation (units: mm), (b) vertical velocity at 500 hPa (units: m s^{-1}), (c) vertical integrated $\boldsymbol{Q}_p$-vector divergence (units: 10^{-4} s^{-2}), (d) vertical integrated $\boldsymbol{Q}_z$-vector divergence (units: 10^{-3} s^{-2}) , (e) $\boldsymbol{Q}_p$-vector divergence at 500 hPa (units: 10^{-8} Pa^{-1} s^{-2}), and (f) $\boldsymbol{Q}_z$-vector divergence at 5.5 km (units: 10^{-6} m^{-1} s^{-2}) along 78°E from 0000 UTC 18 to 0000 UTC 19 July 2021.

the horizontal and vertical direction. By contrast, quasi-geostrophic equilibrium is usually nonexistent in mesoscale systems, and the heterogeneous distribution of water vapor also affects the development of mesoscale systems. Therefore, it is more reasonable and efficient to use generalized vertical motion equations and generalized $\boldsymbol{Q}$ vectors with fewer assumptions in high impact mesoscale systems.

6. Conclusion and discussion

The vertical motion field is one of the key factors in weather analysis and forecasting. The determination of vertical motion commonly depends on the vertical motion equation. For application in mesoscale systems, a new form of generalized vertical motion equation and a generalized Omega equation are derived in this paper within the nonhydrostatic

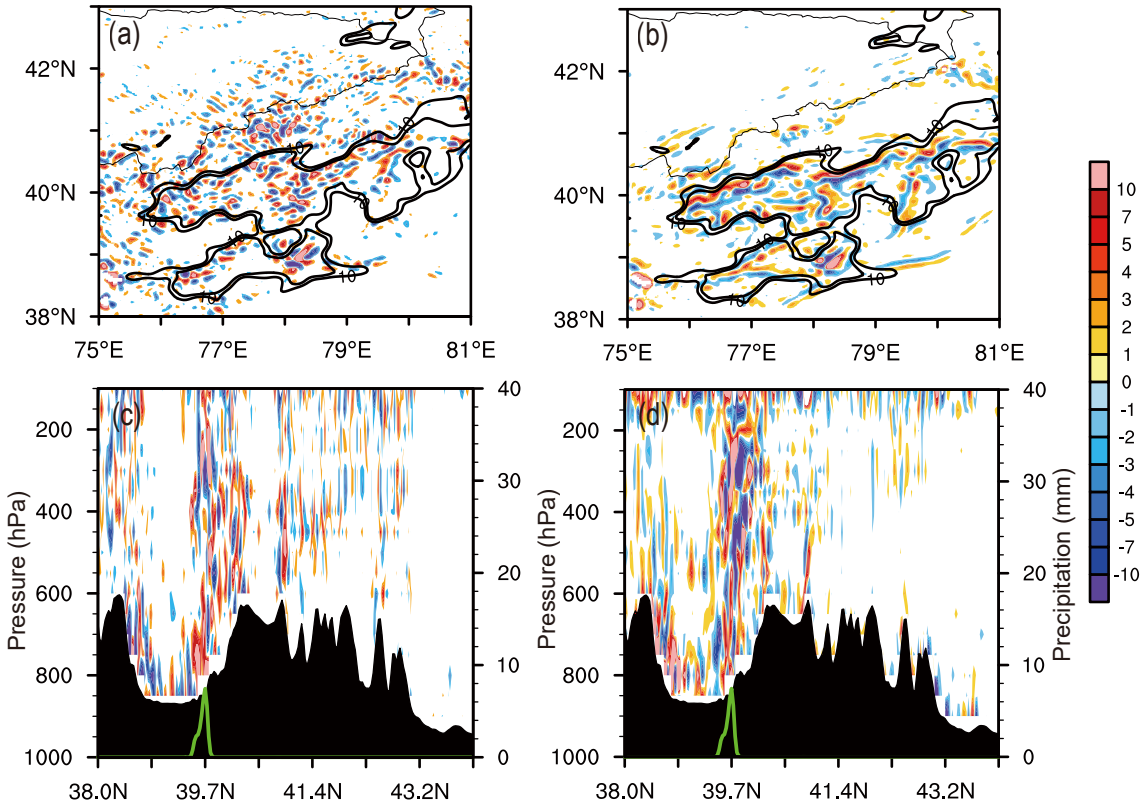

Fig. 9. (a) Horizontal distribution of (a) quasigeostrophic $\boldsymbol{Q}$-vector divergence (units: 10^{-8} Pa^{-1} s^{-3}) and (b) nongeostrophic $\boldsymbol{Q}$-vector divergence (units: 10^{-14} Pa^{-1} s^{-3}) at 500 hPa, and meridional cross sections of (c) quasigeostrophic $\boldsymbol{Q}$-vector divergence and (d) nongeostrophic $\boldsymbol{Q}$-vector divergence along 76°E at 1800 UTC 18 July 2021. The black lines in (a, b) are composite radar reflectivity (units: dBZ), and green solid lines in (c, d) represent hourly precipitation (units: mm).

equilibrium dynamic framework of a local Cartesian coordinate system and the hydrostatic equilibrium framework of the isobaric coordinate system, respectively. Through the forcing terms, namely the $\boldsymbol{Q}$ vector, on the right side of the equations, the physical factors affecting the vertical movement of the left side can be analyzed. According to these derived equations, the $\boldsymbol{Q}$ vector ($\boldsymbol{Q}_z$) of the generalized vertical motion equation contains more thermodynamic information and mass forcing information than the $\boldsymbol{Q}$ vector ($\boldsymbol{Q}_p$) in the generalized Omega equation.

A heavy rain event that occurred 18–19 July 2021 in southern Xinjiang was selected, and the mesoscale numerical model WRF was utilized for high-resolution simulation. Simulated data with high spatial and temporal resolutions were used to analyze the characteristics of the two forms of Q-vector divergence and reveal their relationships with simulated composite radar reflectivity, vertical velocity, and hourly accumulated precipitation.

The main conclusions obtained are described as follows:

1. The $\boldsymbol{Q}_z$- and $\boldsymbol{Q}_p$-vector divergence fields both can indicate the distribution of the vertical motion within the rainband. The horizontal distribution of $\boldsymbol{Q}$-vector divergence is closely related to the composite radar reflectivity, vertical velocity, and hourly accumulated precipitation. The region with high values of $\boldsymbol{Q}_z$-vector divergence had a wider horizontal coverage area and was a better indication for weak precipitation areas.

2. In the vertical structure, the high-value regions of the $\boldsymbol{Q}_z$- and $\boldsymbol{Q}_p$-vector divergence fields at middle levels were closely related to precipitation. The relationship between the high-level abnormal value of the $\boldsymbol{Q}_p$-vector divergence and precipitation was not obvious.

3. The temporal evolution of the vertically integrated $\boldsymbol{Q}_z$-vector divergence was similar to that of the $\boldsymbol{Q}_p$-vector divergence, and both could indicate the development and evolution of the observed rainband.

4. A comparison with the geostrophic and nongeostrophic $\boldsymbol{Q}$ vectors demonstrated that the generalized $\boldsymbol{Q}$ vectors are more informative and consistent in the analysis of mesoscale systems.

The task of quantitative precipitation forecasting continues to challenge numerical models. This paper qualitatively analyzes the relationships between the two forms of $\boldsymbol{Q}$-vector divergence proposed here with vertical motion and precipitation systems. The results demonstrate that the new forms of $\boldsymbol{Q}$ vectors have the potential for tracking and indicating the position and movement of mesoscale precipitation systems. In the future, the quantitative relationship will be addressed based on many experiments among different regions, sea-

sons, and dominant weather patterns. The use of dynamic and statistical methods to process and modify the comprehensive results of numerical forecast products may improve the forecast accuracy of precipitation. Of course, this method is closely related to the performance of the numerical model, especially the forecast of the wind field and temperature, serving as a supplement and/or correction. Additionally, the components of $\boldsymbol{Q}$ vectors are worth further research to reveal the internal dynamic and thermodynamic causes of vertical motion and the development of precipitation systems.

Acknowledgements. This study was supported by the Strategic Priority Research Program of the Chinese Academy of Sciences (Grant No. XDA17010105), National Key Research and Development Program (Grant No. 2018YFC1507104), Science and Technology Development Plan Project of Jilin Province (20180201035SF), Flexible Talents Introducing Project of Xinjiang (2019), and the National Key Scientific and Technological Infrastructure project "Earth System Numerical Simulation Facility" (EarthLab).

APPENDIX A

Derivation of the Generalized Vertical Motion Equation in the Local Cartesian Coordinate System

In the local Cartesian coordinate system, the primitive equations on an f-plane are defined as follows:

$$\frac{\partial u}{\partial t}+u\frac{\partial u}{\partial x}+v\frac{\partial u}{\partial y}+w\frac{\partial u}{\partial z}-f_0v+\frac{1}{\rho}\frac{\partial p}{\partial x}=0\,, \tag{A.1}$$

$$\frac{\partial v}{\partial t}+u\frac{\partial v}{\partial x}+v\frac{\partial v}{\partial y}+w\frac{\partial v}{\partial z}+f_0u+\frac{1}{\rho}\frac{\partial p}{\partial y}=0\,, \tag{A.2}$$

$$\frac{\partial w}{\partial t}+u\frac{\partial w}{\partial x}+v\frac{\partial w}{\partial y}+w\frac{\partial w}{\partial z}+g+\frac{1}{\rho}\frac{\partial p}{\partial z}=0\,, \tag{A.3}$$

$$\frac{\partial \rho}{\partial t}+u\frac{\partial \rho}{\partial x}+v\frac{\partial \rho}{\partial y}+w\frac{\partial \rho}{\partial z}+\rho\left(\frac{\partial u}{\partial x}+\frac{\partial v}{\partial y}+\frac{\partial w}{\partial z}\right)=0\,, \tag{A.4}$$

$$\frac{\partial \theta}{\partial t}+u\frac{\partial \theta}{\partial x}+v\frac{\partial \theta}{\partial y}+w\frac{\partial \theta}{\partial z}=H\,, \tag{A.5}$$

$$\theta=T\left(\frac{p_s}{p}\right)^{\frac{R}{c_p}}\,, \tag{A.6}$$

$$p=\rho RT\,. \tag{A.7}$$

Assuming ρ is a function of altitude, the continuity equation Eq. (A.4) can be simplified as:

$$\frac{\partial u}{\partial x}+\frac{\partial v}{\partial y}+\frac{\partial w}{\partial z}=M_z\,, \tag{A.8}$$

where M_z represents various mass non-conservation terms (the local and advective terms). Using Eq. (A.6) and Eq. (A.7), the pressure gradient can be written as:

$$\frac{\partial p}{\partial x}=\frac{c_p}{c_v}\frac{p}{\theta}\frac{\partial \theta}{\partial x}\,, \tag{A.9}$$

$$\frac{\partial p}{\partial y}=\frac{c_p}{c_v}\frac{p}{\theta}\frac{\partial \theta}{\partial y}\,. \tag{A.10}$$

Thus, the horizontal motion equations can be written as follows:

$$\frac{\partial u}{\partial t}+\boldsymbol{v}_{\rm h}\cdot\nabla u+w\frac{\partial u}{\partial z}-f_0v+h\frac{c_p}{c_v}\frac{\partial \theta}{\partial x}=0\,, \tag{A.11}$$

$$\frac{\partial v}{\partial t}+\boldsymbol{v}_{\rm h}\cdot\nabla v+w\frac{\partial v}{\partial z}+f_0u+h\frac{c_p}{c_v}\frac{\partial \theta}{\partial y}=0\,, \tag{A.12}$$

where $h=R/(p_s/p)^{\frac{R}{c_p}}$.

Geostrophic wind is defined as follows:

$$u_{\rm g}=-\frac{1}{f_0}h\frac{c_p}{c_v}\frac{\partial \theta}{\partial y}\,, \tag{A.13}$$

$$v_{\rm g}=\frac{1}{f_0}h\frac{c_p}{c_v}\frac{\partial \theta}{\partial x}\,. \tag{A.14}$$

Taking $\frac{\partial}{\partial t}+u\frac{\partial}{\partial x}+v\frac{\partial}{\partial y}+w\frac{\partial}{\partial z}$ of Eq. (A.13) and Eq. (A.14), we can obtain the tendency equation of $u_{\rm g}$ and $v_{\rm g}$:

$$\begin{aligned}&\frac{\partial u_{\rm g}}{\partial t}+u\frac{\partial u_{\rm g}}{\partial x}+v\frac{\partial u_{\rm g}}{\partial y}+w\frac{\partial u_{\rm g}}{\partial z}\\&=\frac{h}{f_0}\frac{c_p}{c_v}\left(\frac{\partial u}{\partial y}\frac{\partial \theta}{\partial x}+\frac{\partial v}{\partial y}\frac{\partial \theta}{\partial y}+\frac{\partial w}{\partial y}\frac{\partial \theta}{\partial z}-\frac{\partial H}{\partial y}\right)-\frac{h_{\rm s}}{f_0}\frac{c_p}{c_v}\frac{\partial \theta}{\partial y}\,,\end{aligned} \tag{A.15}$$

$$\begin{aligned}&\frac{\partial v_{\rm g}}{\partial t}+u\frac{\partial v_{\rm g}}{\partial x}+v\frac{\partial v_{\rm g}}{\partial y}+w\frac{\partial v_{\rm g}}{\partial z}\\&=-\frac{h}{f_0}\frac{c_p}{c_v}\left(\frac{\partial u}{\partial x}\frac{\partial \theta}{\partial x}+\frac{\partial v}{\partial x}\frac{\partial \theta}{\partial y}+\frac{\partial w}{\partial x}\frac{\partial \theta}{\partial z}-\frac{\partial H}{\partial x}\right)+\frac{h_{\rm s}}{f_0}\frac{c_p}{c_v}\frac{\partial \theta}{\partial x}\,,\end{aligned} \tag{A.16}$$

where

$$h_{\rm s}=\left(\frac{\partial}{\partial t}+u\frac{\partial}{\partial x}+v\frac{\partial}{\partial y}+w\frac{\partial}{\partial z}\right)h\,. \tag{A.17}$$

Introducing the definition of generalized potential temperature

$$\theta^*=\theta\eta\,, \tag{A.18}$$

where $\eta=L_{\rm v}q_{\rm s}(q_{\rm v}/q_{\rm s})^k/\left(c_pT\right)$ is the latent heat function, Cao et al. (2008) demonstrated that the generalized potential temperature satisfies the following conservation equation:

$$\left(\frac{\partial}{\partial t}+u\frac{\partial}{\partial x}+v\frac{\partial}{\partial y}+w\frac{\partial}{\partial z}\right)\theta^{*}=0\,. \tag{A.19}$$

Using Eqs. (A.18), (A.19), and (A.5), the latent heat function satisfies the following equation:

$$\left(\frac{\partial}{\partial t}+u\frac{\partial}{\partial x}+v\frac{\partial}{\partial y}+w\frac{\partial}{\partial z}\right)\eta=-\frac{\eta}{\theta}H\,. \tag{A.20}$$

Upon substituting Eq. (A.18) into Eq. (A.15) and Eq. (A.16) to replace the potential temperature, the tendency equation of geostrophic wind can be further modified using Eq. (A.17), Eq. (A.19), and (A.20). Subtracting Eq. (A.11) and Eq. (A.12) from the simplified tendency equation of geostrophic wind , we finally obtain the following equations:

$$\begin{aligned}&\left[\frac{\partial v}{\partial y}-h\frac{\partial}{\partial x}\left(\frac{c_p}{c_v f_0\eta}\frac{\partial\theta^{*}}{\partial y}\right)\right]v+\left[\frac{\partial v}{\partial x}-h\frac{\partial}{\partial x}\left(\frac{c_p}{c_v f_0\eta}\frac{\partial\theta^{*}}{\partial x}\right)\right]u+\\&\left(\frac{\partial v}{\partial z}-h\frac{\partial\sigma}{\partial x}\right)w-h\sigma_z\frac{\partial w}{\partial x}+f_0u-\frac{c_p h}{c_v f_0\eta}\left(\frac{\partial u}{\partial x}\frac{\partial\theta^{*}}{\partial x}+\frac{\partial v}{\partial x}\frac{\partial\theta^{*}}{\partial y}\right)+\\&\frac{c_p h}{c_v}\frac{\partial\theta}{\partial y}+\frac{\partial v}{\partial t}+\frac{c_p h}{c_v f_0\eta}\left(\frac{1}{\eta}\frac{\partial\eta}{\partial x}\frac{\partial\theta^{*}}{\partial t}-\frac{\partial^2\theta^{*}}{\partial t\partial x}\right)=0\,,\end{aligned} \tag{A.21}$$

$$\begin{aligned}&\left[\frac{\partial u}{\partial y}+h\frac{\partial}{\partial y}\left(\frac{c_p}{c_v f_0\eta}\frac{\partial\theta^{*}}{\partial y}\right)\right]v+\left[\frac{\partial u}{\partial x}+h\frac{\partial}{\partial y}\left(\frac{c_p}{c_v f_0\eta}\frac{\partial\theta^{*}}{\partial x}\right)\right]u+\\&\left(\frac{\partial u}{\partial z}+h\frac{\partial\sigma}{\partial y}\right)w+h\sigma_z\frac{\partial w}{\partial y}-f_0v+\frac{c_p h}{c_v f_0\eta}\times\\&\left(\frac{\partial u}{\partial y}\frac{\partial\theta^{*}}{\partial x}+\frac{\partial v}{\partial y}\frac{\partial\theta^{*}}{\partial y}\right)+\frac{c_p h}{c_v}\frac{\partial\theta}{\partial x}+\frac{\partial u}{\partial t}+\\&\frac{c_p h}{c_v f_0\eta}\left(\frac{\partial^2\theta^{*}}{\partial t\partial y}-\frac{1}{\eta}\frac{\partial\eta}{\partial y}\frac{\partial\theta^{*}}{\partial t}\right)=0\,,\end{aligned} \tag{A.22}$$

where $\sigma_z=\dfrac{c_p}{c_v f_0\eta}\dfrac{\partial\theta^{*}}{\partial z}$ is the static stability parameter.

Taking the vertical partial derivatives on both sides of Eqs. (A.21) and (A.22), we can obtain

$$\begin{aligned}&-\frac{\partial}{\partial z}(h\sigma_z)\frac{\partial w}{\partial x}+\left[\frac{\partial^2 v}{\partial z^2}-\frac{\partial}{\partial z}\left(h\frac{\partial\sigma_z}{\partial x}\right)\right]w+f_0\frac{\partial u}{\partial z}=\\&q_{zx1}+q_{zx2}+q_{zx3}\,,\end{aligned} \tag{A.23}$$

$$\begin{aligned}&\frac{\partial}{\partial z}(h\sigma_z)\frac{\partial w}{\partial y}+\left[\frac{\partial^2 u}{\partial z^2}+\frac{\partial}{\partial z}\left(h\frac{\partial\sigma_z}{\partial y}\right)\right]w-f_0\frac{\partial v}{\partial z}=\\&-q_{zy1}-q_{zy2}-q_{zy3}\,,\end{aligned} \tag{A.24}$$

The components on the right-hand side of the equations are, respectively:

$$q_{zx1}=-\left(\frac{\partial^2 v}{\partial t\partial z}+u\frac{\partial^2 v}{\partial x\partial z}+v\frac{\partial^2 v}{\partial y\partial z}\right)+\frac{\partial v}{\partial z}\frac{\partial u}{\partial x}-\frac{\partial u}{\partial z}\frac{\partial v}{\partial x}\,, \tag{A.25}$$

$$\begin{aligned}q_{zx2}=&\frac{\partial}{\partial z}\left\{h\frac{c_p}{c_v f_0}\left[\frac{\partial}{\partial x}\left(\frac{1}{\eta}\frac{\partial\theta^{*}}{\partial t}\right)+u\frac{\partial}{\partial x}\left(\frac{1}{\eta}\frac{\partial\theta^{*}}{\partial x}\right)+\right.\right.\\&\left.\left.v\frac{\partial}{\partial x}\left(\frac{1}{\eta}\frac{\partial\theta^{*}}{\partial y}\right)\right]-h\frac{c_p}{c_v}\frac{\partial\theta}{\partial y}\right\}+\frac{c_p h}{c_v f_0}\frac{\partial}{\partial z}\left[\frac{1}{\eta}\left(\frac{\partial u}{\partial x}\frac{\partial\theta^{*}}{\partial x}+\right.\right.\\&\left.\left.\frac{\partial v}{\partial x}\frac{\partial\theta^{*}}{\partial y}\right)\right]+\frac{c_p}{c_v f_0\eta}\frac{\partial h}{\partial z}\left(\frac{\partial u}{\partial x}\frac{\partial\theta^{*}}{\partial x}+\frac{\partial v}{\partial x}\frac{\partial\theta^{*}}{\partial y}\right)\,,\end{aligned} \tag{A.26}$$

$$q_{zx3}=-h\frac{\partial}{\partial x}\left[\sigma_z(\lambda-M_z)\right]-\frac{\partial v}{\partial z}M_z\,, \tag{A.27}$$

$$q_{zy1}=\frac{\partial^2 u}{\partial t\partial z}+u\frac{\partial^2 u}{\partial x\partial z}+v\frac{\partial^2 u}{\partial y\partial z}+\frac{\partial v}{\partial z}\frac{\partial u}{\partial y}-\frac{\partial u}{\partial z}\frac{\partial v}{\partial y}\,, \tag{A.28}$$

$$\begin{aligned}q_{zy2}=&\frac{\partial}{\partial z}\left\{\frac{c_p h}{c_v f_0}\left[\frac{\partial}{\partial y}\left(\frac{1}{\eta}\frac{\partial\theta^{*}}{\partial t}\right)+u\frac{\partial}{\partial y}\left(\frac{1}{\eta}\frac{\partial\theta^{*}}{\partial x}\right)+\right.\right.\\&\left.\left.v\frac{\partial}{\partial y}\left(\frac{1}{\eta}\frac{\partial\theta^{*}}{\partial y}\right)\right]+h\frac{c_p}{c_v}\frac{\partial\theta}{\partial x}\right\}+\\&\frac{c_p h}{c_v f_0}\frac{\partial}{\partial z}\left[\frac{1}{\eta}\left(\frac{\partial u}{\partial y}\frac{\partial\theta^{*}}{\partial x}+\frac{\partial v}{\partial y}\frac{\partial\theta^{*}}{\partial y}\right)\right]+\\&\frac{c_p}{c_v f_0\eta}\frac{\partial h}{\partial z}\left(\frac{\partial u}{\partial y}\frac{\partial\theta^{*}}{\partial x}+\frac{\partial v}{\partial y}\frac{\partial\theta^{*}}{\partial y}\right)\,,\end{aligned} \tag{A.29}$$

$$q_{zy3}=-h\frac{\partial}{\partial y}\left[\sigma_z(\lambda-M_z)\right]+\frac{\partial u}{\partial z}M_z\,. \tag{A.30}$$

Upon subtracting $\frac{\partial}{\partial y}$(A.24)–$\frac{\partial}{\partial x}$(A.23), the generalized vertical motion equation under the Boussinesq approximation in the local Cartesian coordinate system can be obtained as follows:

$$\begin{aligned}&\frac{\partial}{\partial z}(h\sigma_z)\left(\frac{\partial^2 w}{\partial x^2}+\frac{\partial^2 w}{\partial y^2}\right)+f_0\frac{\partial^2 w}{\partial z^2}+\\&\left[-\frac{\partial^2 v}{\partial z^2}+\frac{\partial}{\partial z}\left(2h\frac{\partial\sigma_z}{\partial x}+\sigma_z\frac{\partial h}{\partial x}\right)\right]\frac{\partial w}{\partial x}+\\&\left[\frac{\partial^2 u}{\partial z^2}+\frac{\partial}{\partial z}\left(2h\frac{\partial\sigma_z}{\partial y}+\sigma_z\frac{\partial h}{\partial y}\right)\right]\frac{\partial w}{\partial y}+\\&\left[-\frac{\partial^2\zeta}{\partial z^2}+\frac{\partial^2}{\partial z\partial y}\left(h\frac{\partial\sigma_z}{\partial y}\right)+\frac{\partial^2}{\partial z\partial x}\left(h\frac{\partial\sigma_z}{\partial x}\right)\right]w\\&=-\left(\frac{\partial q_{zx1}}{\partial x}+\frac{\partial q_{zy1}}{\partial y}\right)-\left(\frac{\partial q_{zx2}}{\partial x}+\frac{\partial q_{zy2}}{\partial y}\right)-\\&\left(\frac{\partial q_{zx3}}{\partial x}+\frac{\partial q_{zy3}}{\partial y}\right)+f_0\frac{\partial M_z}{\partial z}\,.\end{aligned} \tag{A.31}$$

APPENDIX B

Derivation of the Generalized Omega Equation in an Isobaric Coordinate System

The primitive equations in the isobaric coordinate system with the *f*-plane approximation can be written as follows:

$$\frac{\partial u}{\partial t}+u\frac{\partial u}{\partial x}+v\frac{\partial u}{\partial y}+\omega\frac{\partial u}{\partial p}-f_0 v=-\frac{\partial \phi}{\partial x}, \tag{B.1}$$

$$\frac{\partial v}{\partial t}+v\frac{\partial v}{\partial x}+v\frac{\partial v}{\partial y}+\omega\frac{\partial v}{\partial p}+f_0 u=-\frac{\partial \phi}{\partial y}, \tag{B.2}$$

$$\frac{\partial u}{\partial x}+\frac{\partial v}{\partial y}+\frac{\partial \omega}{\partial p}=M_p, \tag{B.3}$$

$$\frac{\partial \theta}{\partial t}+u\frac{\partial \theta}{\partial x}+v\frac{\partial \theta}{\partial y}+\omega\frac{\partial \theta}{\partial p}=H, \tag{B.4}$$

$$\frac{\partial \phi}{\partial p}+\alpha=0, \tag{B.5}$$

$$\alpha=\frac{1}{\rho}, \tag{B.6}$$

$$\theta=T\left(\frac{p_s}{p}\right)^{\frac{R}{c_p}}, \tag{B.7}$$

$$p=\rho RT. \tag{B.8}$$

Assuming that the wind is geostrophic $\left(u_{\mathrm{g}},\ v_{\mathrm{g}}\right)$, the following geostrophic balanced relationship is satisfied:

$$-f_0 v_g=-\frac{\partial \phi}{\partial x}, \tag{B.9}$$

$$f_0 u_g=-\frac{\partial \phi}{\partial y}. \tag{B.10}$$

Taking the vertical partial derivative of both sides of the above equations, the thermal wind relationship can be obtained as follows:

$$\frac{\partial u_{\mathrm{g}}}{\partial p}=\frac{h}{f_0}\frac{\partial \theta}{\partial y}, \tag{B.11}$$

$$\frac{\partial v_{\mathrm{g}}}{\partial p}=-\frac{h}{f_0}\frac{\partial \theta}{\partial x}, \tag{B.12}$$

where $h=R(p_{\mathrm{s}}/p)^{-\frac{R}{c_p}}/p=1/(\rho\theta)$

Using the thermal wind balance relations, Eqs. (B.11) and (B.12), the tendency of the vertical shear of the geostrophic wind can be derived as follows:

$$\begin{aligned}&\frac{\partial^2 u_{\mathrm{g}}}{\partial p\partial t}+u\frac{\partial^2 u_{\mathrm{g}}}{\partial p\partial x}+v\frac{\partial^2 u_{\mathrm{g}}}{\partial p\partial y}+\omega\frac{\partial^2 u_{\mathrm{g}}}{\partial p^2}\\&=-\frac{h}{f_0}\left(\frac{\partial u}{\partial y}\frac{\partial \theta}{\partial x}+\frac{\partial v}{\partial y}\frac{\partial \theta}{\partial y}+\frac{\partial \omega}{\partial y}\frac{\partial \theta}{\partial p}-\frac{\partial H}{\partial y}\right)+\frac{\omega}{f_0}\frac{\partial h}{\partial p}\frac{\partial \theta}{\partial y},\end{aligned} \tag{B.13}$$

$$\begin{aligned}&\frac{\partial^2 v_{\mathrm{g}}}{\partial p\partial t}+u\frac{\partial^2 v_{\mathrm{g}}}{\partial p\partial x}+v\frac{\partial^2 v_{\mathrm{g}}}{\partial p\partial y}+\omega\frac{\partial^2 v_{\mathrm{g}}}{\partial p^2}\\&=\frac{h}{f_0}\left(\frac{\partial u}{\partial x}\frac{\partial \theta}{\partial x}+\frac{\partial v}{\partial x}\frac{\partial \theta}{\partial y}+\frac{\partial \omega}{\partial x}\frac{\partial \theta}{\partial p}-\frac{\partial H}{\partial x}\right)-\frac{\omega}{f_0}\frac{\partial h}{\partial p}\frac{\partial \theta}{\partial x}.\end{aligned} \tag{B.14}$$

Taking the vertical partial derivatives of Eqs. (B.1) and (B.2), the vertical wind shear tendency equation can be obtained as follows:

$$\begin{aligned}&\frac{\partial^2 u}{\partial p\partial t}+u\frac{\partial^2 u}{\partial p\partial x}+v\frac{\partial^2 u}{\partial p\partial y}+\omega\frac{\partial^2 u}{\partial p^2}\\&=-\frac{\partial^2 \phi}{\partial p\partial x}-\frac{\partial u}{\partial p}\frac{\partial u}{\partial x}-\frac{\partial v}{\partial p}\frac{\partial u}{\partial y}-\frac{\partial \omega}{\partial p}\frac{\partial u}{\partial p}+f_0\frac{\partial v}{\partial p},\end{aligned} \tag{B.15}$$

$$\begin{aligned}&\frac{\partial^2 v}{\partial p\partial t}+u\frac{\partial^2 v}{\partial p\partial x}+v\frac{\partial^2 v}{\partial p\partial y}+\omega\frac{\partial^2 v}{\partial p^2}\\&=-\frac{\partial^2 \phi}{\partial p\partial y}-\frac{\partial u}{\partial p}\frac{\partial v}{\partial x}-\frac{\partial v}{\partial p}\frac{\partial v}{\partial y}-\frac{\partial \omega}{\partial p}\frac{\partial v}{\partial p}-f_0\frac{\partial u}{\partial p}.\end{aligned} \tag{B.16}$$

The generalized potential temperature is introduced as:

$$\theta^*=\theta\eta, \tag{B.17}$$

where $\eta=L_v q_{\mathrm{s}}(q_v/q_{\mathrm{s}})^k/\left(c_p T\right)$ is the latent heat function. Then, in the isobaric coordinate system, the generalized potential temperature satisfies the following conservation equation:

$$\left(\frac{\partial}{\partial t}+u\frac{\partial}{\partial x}+v\frac{\partial}{\partial y}+\omega\frac{\partial}{\partial p}\right)\theta^*=0. \tag{B.18}$$

Using Eqs. (B.17), (B.18), and (B.4), it can be easily shown that the latent heat function satisfies the following equation:

$$\left(\frac{\partial}{\partial t}+u\frac{\partial}{\partial x}+v\frac{\partial}{\partial y}+\omega\frac{\partial}{\partial p}\right)\eta=-\frac{\eta}{\theta}H. \tag{B.19}$$

Subtracting Eqs. (B.13) and (B.14) from Eqs. (B.15) and (B.16) and then substituting them into Eq. (B.19) yields

$$\begin{aligned}&-\frac{h}{f_0\eta}\frac{\partial \theta^*}{\partial p}\frac{\partial \omega}{\partial y}+\left[-\frac{\partial}{\partial y}\left(\frac{h}{f_0\eta}\frac{\partial \theta^*}{\partial p}\right)+\frac{\partial^2 u}{\partial p^2}\right]\omega-f_0\frac{\partial v}{\partial p}\\&=\frac{\partial u}{\partial p}\frac{\partial v}{\partial y}-\frac{\partial v}{\partial p}\frac{\partial u}{\partial y}+\frac{h}{f_0\eta}\left(\frac{\partial u}{\partial y}\frac{\partial \theta^*}{\partial x}+\frac{\partial v}{\partial y}\frac{\partial \theta^*}{\partial y}\right)+\\&\left[\frac{\partial}{\partial y}\left(\frac{h}{f_0\eta}\frac{\partial \theta^*}{\partial y}\right)-\frac{\partial^2 u}{\partial p\partial y}\right]v+\left[\frac{\partial}{\partial y}\left(\frac{h}{f_0\eta}\frac{\partial \theta^*}{\partial x}\right)-\frac{\partial^2 u}{\partial p\partial x}\right]u+\\&\frac{\partial}{\partial y}\left(\frac{h}{f_0\eta}\frac{\partial \theta^*}{\partial t}\right)-\frac{\partial^2 u}{\partial p\partial t}+h\frac{\partial \theta}{\partial x}-\frac{\partial u}{\partial p}M_p,\end{aligned} \tag{B.20}$$

$$\frac{h}{f_0\eta}\frac{\partial\theta^*}{\partial p}\frac{\partial\omega}{\partial x}+\left[\frac{\partial}{\partial x}\left(\frac{h}{f_0\eta}\frac{\partial\theta^*}{\partial p}\right)+\frac{\partial^2 v}{\partial p^2}\right]\omega+f_0\frac{\partial u}{\partial p}$$
$$=-\frac{\partial u}{\partial p}\frac{\partial v}{\partial x}+\frac{\partial v}{\partial p}\frac{\partial u}{\partial x}-\frac{h}{f_0\eta}\left(\frac{\partial u}{\partial x}\frac{\partial\theta^*}{\partial x}+\frac{\partial v}{\partial x}\frac{\partial\theta^*}{\partial y}\right)-$$
$$\left[\frac{\partial}{\partial x}\left(\frac{h}{f_0\eta}\frac{\partial\theta^*}{\partial y}\right)+\frac{\partial^2 v}{\partial p\partial y}\right]v-\left[\frac{\partial}{\partial x}\left(\frac{h}{f_0\eta}\frac{\partial\theta^*}{\partial x}\right)+\frac{\partial^2 v}{\partial p\partial x}\right]u-$$
$$\frac{\partial}{\partial x}\left(\frac{h}{f_0\eta}\frac{\partial\theta^*}{\partial t}\right)-\frac{\partial^2 v}{\partial p\partial t}+h\frac{\partial\theta}{\partial y}-\frac{\partial v}{\partial p}M_p\,. \tag{B.21}$$

Three sets of $\boldsymbol{Q}$ vectors are defined as: (q_{px1},q_{py1}), (q_{px2},q_{py2}), and (q_{px3},q_{py3}):

$$q_{px1}=\frac{\partial^2 v}{\partial p\partial t}+u\frac{\partial^2 v}{\partial p\partial x}+v\frac{\partial^2 v}{\partial p\partial y}+\frac{\partial u}{\partial p}\frac{\partial v}{\partial x}-\frac{\partial v}{\partial p}\frac{\partial u}{\partial x}\,, \tag{B.22}$$

$$q_{px2}=\frac{h}{f_0}\left[\frac{\partial}{\partial x}\left(\frac{1}{\eta}\frac{\partial\theta^*}{\partial t}\right)+u\frac{\partial}{\partial x}\left(\frac{1}{\eta}\frac{\partial\theta^*}{\partial x}\right)+v\frac{\partial}{\partial x}\left(\frac{1}{\eta}\frac{\partial\theta^*}{\partial y}\right)+\right.$$
$$\left.\frac{1}{\eta}\left(\frac{\partial u}{\partial x}\frac{\partial\theta^*}{\partial x}+\frac{\partial v}{\partial x}\frac{\partial\theta^*}{\partial y}\right)\right]-h\frac{\partial\theta}{\partial y}\,, \tag{B.23}$$

$$q_{px3}=\frac{\partial v}{\partial p}M_p\,, \tag{B.24}$$

$$q_{py1}=-\frac{\partial^2 u}{\partial p\partial t}-u\frac{\partial^2 u}{\partial p\partial x}-v\frac{\partial^2 u}{\partial p\partial y}-\frac{\partial v}{\partial p}\frac{\partial u}{\partial y}+\frac{\partial u}{\partial p}\frac{\partial v}{\partial y}\,, \tag{B.25}$$

$$q_{py2}=\frac{h}{f_0}\left[\frac{\partial}{\partial y}\left(\frac{1}{\eta}\frac{\partial\theta^*}{\partial t}\right)+u\frac{\partial}{\partial y}\left(\frac{1}{\eta}\frac{\partial\theta^*}{\partial x}\right)+v\frac{\partial}{\partial y}\left(\frac{1}{\eta}\frac{\partial\theta^*}{\partial y}\right)+\right.$$
$$\left.\frac{1}{\eta}\left(\frac{\partial u}{\partial y}\frac{\partial\theta^*}{\partial x}+\frac{\partial v}{\partial y}\frac{\partial\theta^*}{\partial y}\right)\right]+h\frac{\partial\theta}{\partial x}\,, \tag{B.26}$$

$$q_{py3}=-\frac{\partial u}{\partial p}M_p\,. \tag{B.27}$$

Substituting Eq. (B.22) minus Eq. (B.27) into Eqs. (B.20) and (B.21), we obtain

$$h\frac{\partial}{\partial x}\left(\sigma_p\omega\right)+\omega\frac{\partial^2 v}{\partial p^2}+f_0\frac{\partial u}{\partial p}=-q_{px1}-q_{px2}-q_{px3}\,, \tag{B.28}$$

$$-h\frac{\partial}{\partial y}\left(\sigma_p\omega\right)+\omega\frac{\partial^2 u}{\partial p^2}-f_0\frac{\partial v}{\partial p}=q_{py1}+q_{py2}+q_{py3}\,, \tag{B.29}$$

where $\sigma_p=\dfrac{1}{f_0\eta}\dfrac{\partial\theta^*}{\partial p}$.

With $\dfrac{\partial}{\partial x}$(B.28)$-\dfrac{\partial}{\partial y}$(B.29), the generalized Omega equation in the isobaric coordinate system can be obtained as follows:

$$\frac{\partial^2}{\partial x^2}\left(\sigma_p\omega\right)+\frac{\partial^2}{\partial y^2}\left(\sigma_p\omega\right)-f_0\frac{\partial^2\omega}{\partial p^2}+\frac{\partial\omega}{\partial x}\frac{\partial^2 v}{\partial p^2}-\frac{\partial\omega}{\partial y}\frac{\partial^2 u}{\partial p^2}+\frac{\partial^2\zeta}{\partial p^2}\omega$$
$$=-\left(\frac{\partial q_{px1}}{\partial x}+\frac{\partial q_{py1}}{\partial y}\right)-\left(\frac{\partial q_{px2}}{\partial x}+\frac{\partial q_{py2}}{\partial y}\right)-\left(\frac{\partial q_{px3}}{\partial x}+\frac{\partial q_{py3}}{\partial y}\right)-$$
$$f_0\frac{\partial M_p}{\partial p}\,, \tag{B.30}$$

where $\zeta=\dfrac{\partial v}{\partial x}-\dfrac{\partial u}{\partial y}$.

REFERENCES

Cao, J., S. T. Gao, and Y. S. Zhou, 2008: Improved Q vector analyses from the perspective of field separation and its application in a torrential rain event. *Acta Physica Sinica*, **57**(4), 2600–2606, https://doi.org/10.7498/aps.57.2600. (in Chinese with English abstract)

Davies-Jones, R., 1991: The frontogenetical forcing of secondary circulations. Part I: The duality and generalization of the Q vector. *J. Atmos. Sci.*, **48**(4), 497–509, https://doi.org/10.1175/1520-0469(1991)048<0497:TFFOSC>2.0.CO;2.

Dixon, M. A. G., A. J. Thorpe, and K. A. Browning, 2003: Layer-wise attribution of vertical motion and the influence of potential-vorticity anomalies on synoptic development. *Quart. J. Roy. Meteor. Soc.*, **129**, 1761–1778, https://doi.org/10.1256/qj.02.83.

Gao, S. T., and Y. S. Zhou, 2019: Progress in dynamics of mesoscale vortex in recent years. *Torrential Rain and Disasters*, **38**(5), 431–439, https://doi.org/10.3969/j.issn.1004-9045.2019.05.005. (in Chinese with English abstract)

Gao, S. T., X. R. Wang, and Y. S. Zhou, 2004: Generation of generalized moist potential vorticity in a frictionless and moist adiabatic flow. *Geophys. Res. Lett.*, **31**(12), L12113, https://doi.org/10.1029/2003GL019152.

Gao, S. T., L. K. Ran, N. Li, and X. Zhang, 2013: The "Ensemble Dynamic Factors" approach to predict rainstorm. *Torrential Rain and Disasters*, **32**(4), 289–302, https://doi.org/10.3969/j.issn.1004-9045.2013.04.001. (in Chinese with English abstract)

Hoskins, B. J., I. Draghici. 1977. The forcing of ageostrophic motion according to the semi-geostrophci equations and in an isentropic coordinate model. *J Atmos Sci*, 34(12): 1859-1867, https://doi.org/10.1175/1520-0469(1977)034<1859:TFOAMA>2.0.CO;2.

Hoskins, B. J., I. Draghici, and H. C. Davies, 1978: A new look at the ω-equation. *Quart. J. Roy. Meteor. Soc.*, **104**(439), 31–38, https://doi.org/10.1002/qj.49710443903.

Li, C. Q., 2018: Research on the application of potential vorticity inversion and generalized vertical. Ph. D. dissertation, Institute of Atmospheric Physics, Chinese Academy of Sciences. (in Chinese)

Räisänen, J., 1995: Factors affecting synoptic-scale vertical motions: A statistical study using a generalized omega equation. *Mon. Wea. Rev.*, **123**(8), 2447–2460, https://doi.org/10.1175/1520-0493(1995)123<2447:FASSVM>2.0.CO;2.

Ran, L. K., Z. Li, Y. B. Zhang, and Y. B. Qi, 2019: The diagnostic analysis of Q vector during a heavy rain event in North China. *Torrential Rain and Disasters*, **38**(1), 17–30, https://doi.org/10.3969/j.issn.1004-9045.2019.01.003. (in Chinese with English abstract)

Rantanen, M., J. Raïsänen, J. Lento, O. Stepanyuk, O. Räty, V. A.

Sinclair, and H. Järvinen, 2017: OZO v.1.0: Software for solving a generalised omega equation and the Zwack-Okossi height tendency equation using WRF model output. *Geoscientific Model Development*, **10**(2), 827–841, https://doi.org/10.5194/gmd-10-827-2017.

Shen, Y., Y. Pan, J. J. Yu, P. Zhao, and Z. J. Zhou, 2013: Quality assessment of hourly merged precipitation product over China. *Transactions of Atmospheric Sciences*, **36**(1), 37–46, https://doi.org/10.13878/j.cnki.dqkxxb.2013.01.005. (in Chinese with English abstract)

Strahl, J. L. S., and P. J. Smith, 2001: A diagnostic study of an explosively developing extratropical cyclone and an associated 500-hPa trough merger. *Mon. Wea. Rev.*, **129**(9), 2310–2328, https://doi.org/10.1175/1520-0493(2001)129<2310:ADSOAE>2.0.CO;2.

Vasilj, J. M., and P. J. Smith, 1997: A comparison of extended and quasigeostrophic dynamics for a case of small-rossby number extratropical cyclone development. *Mon. Wea. Rev.*, **125**(12), 3347–3356, https://doi.org/10.1175/1520-0493(1997)125<3347:ACOEAQ>2.0.CO;2.

Xu, Q., 1992: Ageostrophic pseudovorticity and geostrophic C-vector forcing—A new look at the Q vector in three dimensions. *J. Atmos. Sci.*, **49**(12), 981–990, https://doi.org/10.1175/1520-0469(1992)049<0981:APAGCV>2.0.CO;2.

Yang, S., S. T. Gao, and D. H. Wang, 2007: Diagnostic analyses of the ageostrophic $\vec{Q}$ vector in the non-uniformly saturated, frictionless, and moist adiabatic flow. *J. Geophys. Res.: Atmos.*, **112**(D9), D09114, https://doi.org/10.1029/2006JD008142.

Yao, X. P., Y. B. Yu, and S. W. Shou, 2004: Diagnostic analyses and application of the moist ageostrophic vector *Q*. *Adv. Atmos. Sci.*, **21**(1), 96–102, https://doi.org/10.1007/BF02915683.

Yue, C. J., 2014: Progress in application study of Q vector, helicity, potential vorticity and its inversion to torrential rainfall associated with typhoon. *Torrential Rain and Disasters*, **33**(3), 193–201, https://doi.org/10.3969/j.issn.1004-9045.2014.03.001. (in Chinese with English abstract)

Yue, C. J., J. Li, P. Y. Chen, T. Xu, and X. F. Wang, 2013: Study on improvement of moist Q vector interpretation technique. *Plateau Meteorology*, **32**(6), 1617–1625, https://doi.org/10.7522/j.issn.1000-0534.2012.00155. (in Chinese with English abstract)

Zhu, Q. G., J. R. Lin, S. W. Shou, 2007: *Principles and Methods of Meteorology*. 619–636. (in Chinese)